The impact of astronomical forcing on the Late Devonian greenhouse climate

David De Vleeschouwer[1], Michel Crucifix[2], Nabila Bounceur[2], Philippe Claeys[1]

[1] Earth System Sciences and Department of Geology, Vrije Universiteit Brussel, Pleinlaan 2, B -1050 Brussels, Belgium
[2] Georges Lemaître Centre for Earth and Climate Research, Earth and Life Institute, Université catholique de Louvain, Louvain-la-Neuve, Belgium

Corresponding author: David De Vleeschouwer (dadevlee@gmail.com)

HIGHLIGHTS

- Application of a General Circulation Model to represent Late Devonian climates
- First-order estimate of Late Devonian climate response to astronomical forcing
- Use of model simulations to better interpret cyclic features in the geologic record
- A link between ocean anoxia and simultaneously high eccentricity and obliquity

1. Abstract

The geological record of the Paleozoic often exhibits cyclic features, in many cases the result of changes in paleoclimate. However, a thorough understanding of the processes that were driving Paleozoic climate change has not yet been reached. The main reason is relatively poor time-control on Paleozoic paleoclimate proxy records. This problem can be overcome by the identification of cyclic features resulting from astronomical climate forcing in the stratigraphic record. To correctly identify these cyclic features, it is necessary to quantify the effects of astronomical climate forcing under conditions different from today. In this work, we apply Late Devonian (375 Ma) boundary conditions to the Hadley Centre general circulation model (HadSM3). We estimate the response of Late Devonian climate to astronomical forcing by keeping all other forcing factors (e.g. paleogeography, $p\mathrm{CO}_2$, vegetation distribution) fixed. Thirty-one different "snapshots" of Late Devonian climate are simulated, by running the model with different combinations of eccentricity (e), obliquity (ε) and precession ($\tilde{\omega}$). From the comparison of these 31 simulations, it appears that feedback mechanisms play an important role in the conversion of astronomically driven insolation variations into climate change, such as the formation of sea-ice and the development of an extensive snow cover on Gondwana. We compare the "median orbit" simulation to lithic indicators of paleoclimate to evaluate whether or not HadSM3 validly simulates Late Devonian climates. This comparison suggests that the model correctly locates the major climate zones. This study also tests the proposed link between the formation of ocean anoxia and high eccentricity (De Vleeschouwer et al. 2013) by comparing the $\delta^{18}O_{carb}$ record of the Frasnian - Famennian boundary interval from the Kowala section (Poland) with a simulated time series of astronomically-forced changes in mean annual temperature at the paleolocation of Poland. The amplitude of climate change suggested by the isotope record is greater than that of the simulated climate. Hence,

astronomically-forced climate change may have been further amplified by other feedback mechanisms not considered here (e.g. CO_2 and vegetation). Finally, the geologic and simulated time series correlate best when the Frasnian - Famennian negative isotope excursion aligns with maximum mean annual temperature in Poland, which is obtained when eccentricity and obliquity are simultaneously high. This finding supports a connection between Devonian ocean anoxic events and astronomical climate forcing.

Key Words

Late Devonian, astronomical forcing, General Circulation Model, HadSM3, precession, obliquity

2. INTRODUCTION

Most of the Devonian Period is dominated by warm greenhouse climate conditions (Copper, 2002; Joachimski et al., 2009). The geologic record of this 60-Myr long period shows evidence for both long-term (Myr-scale) and abrupt climate variability, together with substantial changes in biodiversity. During the Late Devonian (382.7 - 358.9 Ma; Becker et al., 2012) intense environmental change led to the Frasnian - Famennian (F-F) mass extinction event. This event is one of the "Big Five" extinction events in the Phanerozoic and decimated most of the warm-water reef-builders, such as stromatoporoids, rugose and tabulate corals (McGhee, 1996). In the course of the Late Devonian, the climate transitioned from an extreme greenhouse world (Frasnian) towards an icehouse world (late Famennian; Caputo et al., 2008; Isaacson et al., 2008; Isbell et al., 2003; Streel et al., 2000), coupled with decreasing atmospheric pCO_2 values (Berner, 2006). The gradual closure of the Rheic ocean and the changing planetary albedo due to the colonization of the continents by land plants constitute other important drivers of long-term climate change during the Devonian (Algeo and Scheckler, 1998; Godderis et al., 2014). Multiple Devonian geologic records suggest that, superimposed on the longer-term climatic trends, the effect of astronomical climate forcing can be recognized (e.g. Bai, 1995; Chen and Tucker, 2003; Chlupáč, 2000; Crick et al., 2001; De Vleeschouwer et al., 2012a; 2012b; 2013; Ellwood et al., 2011a; 2011b; House, 1991; 1995). However, a thorough understanding of the mechanisms through which astronomical climate forcing operates in a greenhouse world is still lacking. Consequently, to what degree astronomical climate forcing played a role in triggering the numerous widespread ocean anoxic events of the Devonian remains an open question.

In this study, we use a general circulation model (GCM) to simulate Late Devonian greenhouse climates under different astronomical configurations. We then compare these different simulated climates, and document the climatic changes that are caused by specific astronomical configurations. Subsequently, different types of geologic data (lithic indicators of paleoclimate, $\delta^{18}O_{apatite}$ paleothermometry and astrochronologically-calibrated proxy records) are compared to the model simulations. The objective is, first, to assess the performance of the model in simulating Late Devonian climate, and then to document the mechanisms that control climate sensitivity to astronomical forcing during the Late Devonian greenhouse world. Finally, we compare the Late Devonian climate simulations to cyclic features in the stratigraphic record, with a focus on the possible role of astronomical forcing in the triggering and pacing of Devonian widespread ocean anoxic events.

3. CLIMATE MODEL AND EXPERIMENTAL DESIGN

The general circulation model (GCM) used in this study is the Hadley Centre model HadSM3 in which the atmospheric model is coupled to a slab ocean (Pope et al., 2000; Williams et al., 2001). The Hadley Centre Model has been broadly used for climate prediction (e.g. Bell et al., 2010; Betts et al., 2007; Collins et al., 2006; Kim et al., 2011; Stainforth et al., 2005) as well as for paleoclimate analysis and reconstruction (e.g. Brayshaw et al., 2011; Craggs et al., 2012; Crucifix and Hewitt, 2005; Haywood et al., 2002; Spicer et al., 2008; Tindall et al., 2010). The spatial resolution of HadSM3 (3.75° long x 2.5° lat) is suitable to capture the essential mechanisms and processes of monsoonal systems (Turner et al., 2008). The albedo of accumulating ice and snow is computed according to the MOSES-1 scheme (Cox et al., 1999). For a more detailed description of the model, the reader is referred to Pope et al. (2000).

3.1. ANOMALOUS HEAT CONVERGENCE

Because of the lack of ocean dynamics in a slab ocean model, a corrective heat flux must be calculated to obtain a realistic representation of sea surface temperatures (SSTs) and sea-ice. The calibration of these heat fluxes requires prescribed SSTs, which have been derived by imposing a parabolic decline of SSTs from maximum 32°C in the tropics (Joachimski et al., 2009) to minimum 0°C at the poles. The anomalous heat convergence obtained during this calibration experiment (with ε=23.5° and e=0) is used in all simulations described in this paper.

3.2. TOPOGRAPHY

Similar to a previous GCM study of the Late Devonian (Le Hir et al., 2011), we supply the HadSM3 model with a quantified version of Blakey's (2010) global paleogeographic reconstruction of the Late Devonian (Fig. 1a). The Euramerican orographic barrier has the highest elevation (3000 m) because subduction zones characterized by convergence up to 10 cm/kyr surround this continent (Torsvik et al., 2012). The Gondwanan craton is given a low altitude (200 m), apart from some 1500 m high plateaus in western Gondwana and subduction-related mountain ranges in eastern Gondwana. In North Siberia, an east-west oriented orographic barrier (1500 m) is associated with the subduction zone there (Blakey, 2010; Torsvik et al., 2012).

3.3. SOIL AND VEGETATION DISTRIBUTION

The experiments are conducted without vegetation feedbacks. The same soil and vegetation distribution is considered in all model experiments (as shown in Fig. 1b). A provisional soil and vegetation distribution is obtained by applying the Köppen-Geiger classification scheme to a vegetation-free "median orbit" simulation (with ε=23.5° and e=0), using the MeteoLab toolbox for MATLAB (Cofiño et al., 2004). This provisional distribution is used in a subsequent climate simulation. The obtained surface temperature (T_s) and precipitation (PP) patterns are used for the definitive classification shown in Fig. 1b. Unfortunately, the fragmentary nature of Late Devonian paleobotany data hampers a precise estimate of each of the soil and vegetation parameters. Therefore, the absolute values for all soil and vegetation parameters are taken from corresponding extant soil and vegetation types (see Appendix 1).

3.4. EXPERIMENTAL DESIGN

All experiments are carried out with identical continental distribution and topography (Fig. 1a; Blakey, 2010), solar constant (1324 W/m², faint young Sun; Gough, 1981), *p*CO_2 (2180 ppm; Berner, 2006), soil parameters and vegetation parameters. The astronomical parameters are varied according to the experimental design in Table 1. Each experiment represents a "snapshot" of Late Devonian climate. In total, Late Devonian climates are simulated for 31 different combinations of the three astronomical parameters, eccentricity (e), obliquity (ε) and precession ($\tilde{\omega}$). In this paper, $\tilde{\omega}$ is defined as the heliocentric longitude of perihelion ($\tilde{\omega} = 0°$ implies that perihelion is reached in March). Each experiment is a 40-year simulation run, of which the last 15 years are retained for averaging. Where we refer to regional climates, these were computed by averaging climatic outputs over nine gridboxes.

4. RESULTS

The climate of the Late Devonian "median orbit" experiment is described in detail. In this experiment, the obliquity is 23.5°, close to the present-day value. The shape of the Earth's orbit is circular (i.e. eccentricity equal to 0), such that precession plays no part.

4.1. GLOBAL SURFACE TEMPERATURE PATTERNS

The seasonally averaged T_s for the "median orbit" simulation (Fig. 2) shows that, in this simulation, a large part of Gondwana freezes during austral winter. Negative average winter temperatures occur up to 45-50°S (Fig. 2c). There is only a single gridbox (at 85°S and 2000 meter altitude) where snow and ice survive the summer and where it is possible to form a glacier or ice cap. Considering the significant uncertainty on the applied Late Devonian topography, this simulation suggests that it was possible for Gondwanan mountain glaciers to exist at 2180 ppm pCO_2, provided that they were located at high latitude and altitude. At the tropical latitudes of Gondwana, the highest land temperatures of this "median orbit" simulation occur in January, with a monthly average temperature of 37°C (Fig. 3b). Figure 3b also displays the continental character of Gondwana's climate, with up to 40°C difference in T_s over land between January and July. The simulated Late Devonian SSTs are significantly higher than the modern pre-industrial ones, following the choice that was made in the calibration run. At 60°S the difference in SST between the Late Devonian and pre-industrial simulations is 13°C, whereas at the equator it is only 1.2°C (Fig. 3a). This means that the pole-to-equator temperature gradient of this "median orbit" Late Devonian climate is rather low, similar to what is reported for more recent greenhouse climates (e.g. Bijl et al., 2009; Littler et al., 2011).

4.2. GLOBAL WIND AND PRECIPITATION PATTERNS

The Intertropical Convergence Zone (ITCZ) is highlighted in the horizontal distribution of winds and pressure cells near the surface for December-January-February (DJF) and June-July-August (JJA; Fig. 4). Maximum precipitation rates are attained over the Paleo-Tethys Ocean during austral summer (DJF; Fig. 5). During that season, prominent thermal lows form over the northern regions of Gondwana (Fig. 4a) in response to intensive solar heating of the land surface. Another thermal low emerges in the southwestern part of Euramerica and induces the southward kink of the ITCZ during DJF. The boreal summer (JJA) has low-pressure cells over northeastern Euramerica and Siberia, which result in the prominent S-shape of the ITCZ (Fig. 4b). Intense precipitation in the summer hemisphere during either solstice is accompanied by drought in the subtropics of the winter hemisphere (Figs. 5a,c), associated with the intensification of the subtropical high-pressure cells during winter (Fig. 4). During DJF, moisture-bearing trade winds enter the Euramerican continent in the west, travel southeast, and progressively lose their moisture content over the southwestern part of the continent (Figs. 4a,5a). Around the equinoxes, a strong thermal low develops in central and northern Euramerica, such that moist air originating from the northern Paleo-Tethys in the northeast and the Rheic Ocean in the southeast is forced to rise. This convective motion results in twice-yearly precipitation maxima in equatorial Euramerica (Figs. 5b,d).

The Late Devonian latitudinal distribution of mean annual precipitation rate is compared to that of a pre-industrial simulation in Fig. 6a. This comparison shows that Late Devonian ITCZ-related intense precipitation extends over a wider range of latitudes than the pre-industrial one (Fig. 6a). At high and mid-latitudes, mean annual precipitation is generally higher in the Late Devonian simulation that in the pre-industrial one. Late Devonian intertropical precipitation is characterized by strong seasonality, associated with the annual migration of the ITCZ (Fig. 6b). The solstitial precipitation maximum in the northern hemisphere (NH; July) is higher and more confined compared to the southern hemispheric (SH; January) one. This characteristic is the result of the ITCZ migrating over a wider latitudinal range in the SH, where most of the continental land mass is concentrated.

4.3. MONSOONAL SYSTEMS

A monsoon climate is characterized by a single solstitial rainfall maximum and prevailing wind directions that shift by at least 120° between winter and summer. Monsoon regions for which these two criteria apply are shown in Fig. 7. Four different monsoon systems can be distinguished: a southern Siberian, a Paleo-Tethys, a southeastern Euramerican and a southwestern Euramerican monsoonal system. Because of the strong concentration of continents in the SH, the monsoon region in the SH covers a considerably wider latitudinal range than in the NH. During summer, the monsoonal system in southern Siberia is characterized by westerly winds, flowing to the south of the thermal low that develops in the center of the Siberian continent. These westerlies advect warm and moist air, providing ~100 mm/month precipitation. During winter, a high-pressure cell develops on the continent, so that winds flow from east to west over southern Siberia. This relatively cold and dry air only allows for 10-50 mm precipitation per month. The monsoonal system of southwestern Euramerica receives warm and moist trade winds from over the Panthalassic Ocean during austral summer (~150 mm/month). In JJA, the subtropical high over the Rheic Ocean causes anticyclonic flow over southern Euramerica, so that dry continental air reaches southwestern Euramerica from the southeast. The southeastern Euramerican monsoonal system has a very similar winter circulation. However, during summer, the wet and moist air that reaches southeastern Euramerica is advected from the Paleo-Tethys Ocean in the northeast. In the Paleo-Tethys monsoonal system, warm and moist northwesterly trade winds deliver precipitation during the DJF wet season. The wind pattern during the dry season, on the other hand, is steered by the strong high-pressure cell above northeastern Gondwana. The latter induces the advection of relatively cold and dry air from the southeast. The climate in the northern part of the Euramerican continent does not meet the definition of a monsoon climate, as it is characterized by twice-yearly rainfall maxima, occurring around the equinoxes.

4.4. The impact of precession and obliquity on Late Devonian surface temperature and precipitation.

To investigate the influence of precession and obliquity on the Late Devonian climate, we analyze the differences in global T_s and PP patterns between [1] two opposite precessional configurations and [2] maximum and minimum obliquity. In the first case, we compare Earth at perihelion in December (*xaclm*) with Earth at perihelion in June (*xaclo*), under moderate obliquity ε=23.5° and high eccentricity e=0.07. In the second case, we compare ε=24.5° (*xaclg*) with ε=22°, (*xaclb*) under a circular orbit (e=0).

Precession-induced changes in surface temperature are largest over landmasses for all seasons (Fig. 8). Maximum response is located over northern Gondwana in DJF. During September-October-November (SON), maximum response is located over southern Gondwana (Fig. 8d). During JJA, the effect is largest over Siberia, Euramerica and northernmost tropical Gondwana (Fig. 8c). When perihelion is reached in December (*xaclm*), the seasonality of incoming solar radiation is enhanced in the SH and decreased in the NH. The opposite occurs when perihelion is reached in June (*xaclo)*. The patterns of simulated DJF and JJA temperature response (Figs. 8a,c) consistently show enhanced SH seasonality in *xaclm*, and enhanced NH seasonality in *xaclo*. The temperature response is thus generally positively correlated with the forcing. However, in Euramerica and northernmost Gondwana the temperature response to the applied forcing in DJF is small or opposite to the forcing (Fig. 8a). This feature is related to the monsoonal response. When the Earth reaches perihelion in December, the enhanced incoming solar energy during DJF causes a strong increase in cloud cover, precipitation (Fig. 9) and evaporation over Euramerica and therefore, more incoming radiation is used as latent heat. Further, the increased cloud cover influences the radiation balance. Figures 10a and 10b show the net cloud radiative forcing (NetCRF), normalized for incoming solar radiation at the top of the atmosphere (TOA) for respectively experiment *xaclm* and *xaclo*. The NetCRF results from two opposite effects: the reflective character of clouds contributing to the planetary albedo and the longwave absorption contributing to the greenhouse effect. The NetCRF is simply the sum of both counteracting effects and is defined as

$$NetCRF = R_C - R + F_C - F$$

where R denotes TOA all-sky reflected shortwave radiation and R_C that of clear skies. F and F_C, respectively, denote the all-sky and clear-sky TOA emitted longwave radiation. When the Earth reaches perihelion in December (*xaclm*), the normalized NetCRF above Euramerica is more negative than when the Earth reaches perihelion in June (*xaclo*). This means that a more dense DJF cloud cover in *xaclm* instigates a negative albedo feedback mechanism that further contributes to lower summer temperatures in Euramerica.

Between the two precessional configurations that are compared here, the largest differences in insolation forcing occur at the solstices. Nevertheless, it is in austral spring (SON) that the largest temperature response is observed, with a strong surface temperature response in Gondwana (Fig. 8d and purple line on Fig. 10c). This amplification is the result of a positive snow-albedo feedback mechanism. Indeed, when the Earth is at perihelion in December, it is relatively far from the sun during SH winter and spring (June till October). This astronomical configuration implies a lower amount of incoming solar radiation in the SH during SON. The irradiance deficit prevents a rapid meltdown of the winter snow cover and allows the Gondwanan snow cover to survive until later in austral spring (blue line on Fig. 10c). This high-albedo cover ensures that a larger part of the incoming solar radiation (green line on Fig.

10c) is reflected, at the expense of the amount of absorbed solar energy (and thus temperature; purple line on Fig. 10c).

Figure 9 shows the difference in precipitation patterns between the two opposite precessional configurations and indicates that the position of the ITCZ is significantly influenced. During DJF and March-April-May (MAM), this latitudinal band of intensive precipitation is located further south when the Earth reaches perihelion in December compared to perihelion in June (Figs. 9a, b), in response to the warm anomaly in Gondwana (Fig. 8a,b). Conversely, in JJA, the cold anomaly in Siberia restrains the latitudinal range of the ITCZ and results in a more southerly position of the intensive precipitation belt when Earth reaches perihelion in December (Fig. 9c).

With increasing obliquity, the amount of insolation received at higher latitudes during summer increases at the expense of insolation received by the low and mid-latitudes of the winter hemisphere. The warming at the South Pole during DJF and at the North Pole during JJA is a direct response to this insolation forcing (Figs. 11a,c). The largest temperature increases occur near the poles, which is consistent both with the signature of insolation changes induced by obliquity, and the general mechanism of polar amplification that characterizes the climate system (Alexeev et al., 2005; Holland and Bitz, 2003). The largest warming is found in the northern hemisphere during DJF (up to 8°C difference between obliquity maximum and minimum; Fig. 11a). In the high-obliquity configuration, the positive summer insolation anomaly translates into a positive temperature anomaly, with a summer SST of 13.9°C over the North Pole. Because of the thermal inertia of the oceans, no seasonal sea-ice forms during the subsequent winter and a year-round positive temperature anomaly occurs, despite the small decrease in winter insolation. During an obliquity minimum, summer

SST over the North Pole is only 7.4°C and seasonal sea-ice forms in winter, extending to 70°N.

In the SH polar regions, seasonal sea-ice also appears under obliquity minima, but the resulting effect has a smaller amplitude than in the NH. Namely, SH high-latitude SSTs are ~3°C higher than in the NH (Fig. 3a) and the maximum sea-ice extent is limited to 80°S.

The equatorial rainbelt also responds to obliquity changes. Recall that an increase in obliquity induces an increase in seasonal contrast outside the tropical areas. In fact, during an obliquity maximum, a warm anomaly on the Gondwanan continent is observed during SH summer (DJF; Fig. 11a) which enhances the Euramerican and Paleo-Tethys monsoonal systems (Fig. 12a). Conversely, in JJA, summer precipitation in southern Siberia is enhanced (Fig. 12c) in response to the warm anomaly over that continent (Fig. 11c).

4.5. CLIMATE RESPONSE TO ASTRONOMICAL FORCING

The effect of astronomical forcing on Late Devonian climate is further investigated on the basis of 31 climate simulations covering different combinations of obliquity (ε), and precession ($e \cdot \sin\tilde{\omega}$ and $e \cdot \cos\tilde{\omega}$). Specifically, the response of T_s or PP is depicted by means of two orthogonal cross-sections of the 3-D input space (Figs. 13 and 14). As $\tilde{\omega}$ is defined as the heliocentric longitude of perihelion, the Earth reaches perihelion during the NH summer half year when $\sin\tilde{\omega} > 0$ and vice versa. Perihelion is reached in March when $\cos\tilde{\omega} = 1$ and in September when $\cos\tilde{\omega} = -1$. The response plots in function of $e \cdot \cos\tilde{\omega}$ and $e \cdot \sin\tilde{\omega}$ can thus be viewed as polar plots of which the azimuth represents the longitude of the perihelion and the distance from the pole represents eccentricity. The pole corresponds thus to zero eccentricity. The month during which the Earth reaches perihelion is indicated at the corresponding azimuth to facilitate the interpretation. The cross-sections (Figs. 13 and 14) were estimated based on triangular interpolation between the scattered model-run results.

Global mean annual temperature and precipitation respond almost identically to astronomical forcing (Fig. 13). Global mean annual temperature varies between 19.5 and 27°C, and the global precipitation rate lies between 96 and 114 mm/month. The warmest global climates are induced during periods of high obliquity and eccentricity and are characterized by the most intense hydrological cycle. The warmest and wettest Late Devonian global climates are obtained when high obliquity and eccentricity are combined with $\tilde{\omega} = 180°$ (Earth at perihelion in September). This configuration results in a early seasonal melt of the Gondwanan winter snow cover, the latter acting as a positive feedback. Cold and dry global climates are obtained when the Earth's orbit is circular (zero-eccentricity) or when obliquity is low. Under such astronomical configurations, the Gondwanan winter snow cover is maintained well into the austral spring, increasing the Earth's albedo and thus cooling global climate. Note that the coldest global climate is not exactly found at zero eccentricity. The lowest global temperature and precipitation rate occur at low eccentricity with Earth at aphelion during austral winter (JJA; slightly negative $e \cdot \sin \tilde{\omega}$; Fig. 13c). This configuration corresponds to severe Gondwanan winters and allows for the growth of a thick and extensive snow cover. Because of its thickness and extent, the latter only melts late in the following spring and summer. At higher eccentricity, seasonality is enhanced with Earth at aphelion during JJA and the winter snow cover in central Gondwana grows ~25% thicker. However, under this configuration, maximum Gondwanan summer temperatures counterbalance the most severe Gondwanan winters, causing mean annual global temperature to be moderate.

The model simulations also allow for the evaluation of regional climate responses to astronomical forcing. As an example, we discuss the regional climate response of the southeastern coast of Euramerica, characterized by a monsoonal climate. Here, the wet season is dominated by north-northeastern winds from October till March and the dry season is dominated by southeastern winds from April till September (Fig. 7). The precipitation response in this region differs significantly from the temperature response (Fig. 14). Mean annual temperature exhibits a quadratic response to precessional forcing (Figs. 14a,c), whereas mean annual precipitation shows an exponential response (Figs. 14b,d). The mean annual temperature response in SE Euramerica (Figs. 14a,c) largely mimics the response of mean annual global temperature (Figs. 13a,c), and is thus strongly influenced by the response of Gondwanan winter snow cover to the astronomical forcing. The mean summer (DJF) temperature response is also characterized by a quadratic response to precessional forcing (Figs. 14e,g). When the Earth is at aphelion during austral summer (perihelion in June, $\tilde{\omega} = 90°$), summer (DJF) insolation in this region is minimum. Nevertheless, temperature increases towards the most positive values along the "$e \cdot \sin\tilde{\omega}$"-axis. This pattern is interpreted as a latent heat effect. Given the significantly drier climate when summer insolation is minimum, less heat is consumed for evaporation and, as discussed earlier, cloud albedo feedbacks enhance this effect. Obliquity has little effect on temperature and precipitation in this tropical region (Figs. 14e,f).

5. Discussion

5.1. Model caveats

The simulation of a 375 million year old climate calls for a discussion of the numerous uncertainties involved. The paleotopography used as a boundary condition in this study is undoubtedly a rough simplification of reality. Even if our paleotopography comes fairly close to reality at a given moment during the Late Devonian, still it is not representative of the entire duration of this period. Previous paleoclimate modeling studies indicated that low-latitude orographic barriers impede ITCZ migration (Otto-Bliesner, 1993; 2003; Peyser and Poulsen, 2008). In our Late Devonian experiments, the low-latitude orographic barrier in Euramerica is set at 3000 meters. An increase in the height of this barrier could lead to a decrease in the seasonality of low-latitude precipitation, and vice versa.

Likewise, the distribution of vegetation types was left unchanged throughout the different simulations. As a result, we ignore some important climate feedback mechanisms related to vegetation. For example, if a dynamic vegetation model was used, ecosystems would shift in response to astronomically forced climate change (e.g. Crucifix et al., 2005; Crucifix and Hewitt, 2005) and so would the corresponding transpiration capabilities and albedo. Considering that these two climate-influencing properties vary greatly between different ecosystems, the use of a dynamic vegetation model would influence the climate simulations results. Unfortunately, little is known about Late Devonian ecosystem dynamics, but most likely these were quite different from today. Therefore, we choose to keep the distribution of vegetation unchanged. For the same reason, we consider $p\mathrm{CO}_2$ as constant.

We used a slab model rather than a dynamic ocean model to avoid numerous additional problems (e.g. presence of multiple equilibria, unknown bathymetry and sensitivity to gateways). One caveat is that, by design, the ocean heat transport is constant and cannot compensate for changes in insolation pattern. Therefore, the response of sea-surface temperatures to astronomical forcing is probably larger in a slab ocean model than in a ocean circulation model.

5.2. Data-model comparison

Before making a detailed data-model comparison, we evaluate whether or not the "median orbit" simulation yields meaningful results. This is done by comparing evaporation minus precipitation (E-P) in this simulation with lithic indicators of paleoclimate (Fig. 15). Lithic indicators for different climate zones occur closely together, for example in eastern Gondwana or southwestern Euramerica. The lithic data shown in figure 15 represent a collection of data throughout the entire Late Devonian. It is thus certainly characterized by a considerable amount of noise, generated by both long-term and short-term climate change. Yet, these data still allow for a rough delineation of the major climate zones (Scotese and Barrett, 1990). The major climate zones, highlighted by the lithic indicators, are compared to the position of the major climate zones in the simulated climates to evaluate whether HadSM3 succeeds in simulating reasonable climates for the Late Devonian.

Evaporites are indicative of arid climatic conditions and have been found in Late Devonian stratigraphic records from Canada, Siberia, the East European (Russian) platform and Western Australia (Hurley and Van der Voo, 1987; Meyerhof, 1970; Scotese and Barrett, 1990; Witzke, 1990). These localities are indicated by yellow triangles on figure 15 and concentrate in regions where evaporation exceeds precipitation in the "median orbit" simulation. Indicators for a humid tropical climate (coals and bauxites) occur in the Canadian Arctic, southern China, and the northern margin of the East European (Russian) platform (Embry and Klovan, 1972; Han, 1989; MacNeil and Jones, 2006; Mordberg, 1996; Scotese, 2004; Volkova, 1994; Witzke, 1990). The coals of the Canadian Arctic (northwestern Euramerica) and southern China (Paleo-Tethys) concur with simulated tropical climates. In the East European platform (northeastern Euramerica), evaporites and bauxites are found at relatively short distances, which suggests that this region lies in the transition area between a tropical wet climate to the south and a subtropical arid climate to the north. However, in the "median orbit" simulation, the transition from excess precipitation to excess evaporation occurs further to the south than suggested by the paleoclimate lithic indicators. The northern part of the Canning basin in Australia is attributed to the humid tropical belt by Heckel and Witzke (1979), whereas in the southern part of the basin, sabkha evaporitic deposits are observed. The northern part of the Canning basin corresponds to the northeastern tip of Gondwana, a region for which the "median orbit" simulation predicts tropical climate conditions (Fig. 15). A few degrees south from this position, the model simulates arid and semi-arid climate conditions. Here, the simulated latitudinal climate gradient fits well with the observations. The southwestern tip of the Euramerican continent corresponds to the present-day northeast of the United States. In the latter case, paleobotanic evidence support a floodplain landscape (Cressler et al., 2010). A Late Devonian wetland environment in this region is confirmed by coals (Scheckler, 1986) and palustrine deposits (Dunagan and Driese, 1999). These elements indicate a warm temperate climate, which is in accordance with the paleoclimate model, as this region is located in the transition zone from arid climates in the north to mild mid-latitude climates in the south. In summary, this comparison indicates that the climate model estimates reasonably well the width of the humid tropical belt and the latitudinal position of the transition between tropical and subtropical climates.

Oxygen isotope ($\delta^{18}O_{apatite}$) paleothermometry allows for a more quantitative evaluation of the model sensitivity. Joachimski et al. (2009) constructed a composite oxygen isotope curve for the Devonian based on the analysis of fossil conodont apatite. As our modeling study focuses on the greenhouse climate of the Late Devonian, we compare the climate simulations to the $\delta^{18}O_{apatite}$ paleothermometry of the Late Frasnian. In their paper, Joachimski et al. (2009) built the composite with data from sections in Germany, France and Iowa for the interval between 378.6 and 374.6 Ma. In the German sections, 71 conodont $\delta^{18}O_{apatite}$ measurements range between 16.7 and 19‰ (V-SMOW, analytic precision ±0.2‰, 1σ), which translates in surface water paleotemperatures between 26 and 36°C (Kolodny et al., 1983). As these values come from a 4-Myr long interval, this broad range results from the combination of astronomically forced climate change and climate change on longer time scales. Therefore, the isotopic range in itself is not very instructive. A better comparison can be made when the mean and variance of the $\delta^{18}O_{apatite}$ data is considered. The mean of the 71 measurements is 17.9‰, suggesting a paleotemperature of 30.5°C and the standard deviation (after linear detrending) is 0.49‰ (i.e. 2.1°C). By removing the linear trend, we minimize the contribution of long-term climate change to the variance and obtain a more reliable estimate of the variance in the Milankovitch band. To compare the mean and variance of the $\delta^{18}O_{apatite}$ data with our climate simulations, we generate a regional T_s time series, based on our climate simulations, of which the mean and variance can be calculated. This is done by considering a *hypothetical* astronomical solution, which represents a realistic evolution of the different astronomical parameters over Devonian time. The use of a hypothetical astronomical solution is needed because the Earth's orbital elements cannot be calculated back into the Devonian (Laskar et al., 2011). Eccentricity periods are considered constant throughout the Phanerozoic (Berger et al., 1992), therefore, we use the eccentricity configurations of the last 10 Myr (Fig. 16a; Laskar et al., 2004). Calculations by Berger et al. (1992) suggest that the shortening of the Earth-moon distance and of the length of the day back in time induced shorter fundamental periods of obliquity and precession in the Devonian. We shortened the periodicities of respectively obliquity and precession in La2004 (Laskar et al., 2004) by 21% and 12% (according to the calculations of Berger et al., 1992) to obtain a hypothetical 10-Myr long series of astronomical configurations for the Late Devonian. Subsequently, for every single astronomical configuration in this series, the mean annual temperatures at the paleolocations of Germany, France and Iowa are estimated, using the 3-D regional climate response for those locations (similar to the 3-D climate response for southeast Euramerica shown in Figs. 14a,c). In this way, we obtain three 10-Myr long simulated time-series of astronomically-forced mean annual temperature. The time series for the paleolocation of Germany has a mean of 27.6°C and a standard deviation of 0.66°C. The $\delta^{18}O_{apatite}$ data for France and Iowa are summarized in Table 2 and compared to the average and standard deviation of the 10-Myr long mean annual temperature series for those paleolocations. In all three cases, the simulated temperatures are several degrees lower than the temperatures suggested by the oxygen isotopes. The reason for this discrepancy is unknown. It can be due to biases in the isotopic thermometer as well as climate simulations inaccuracies (see model caveats). For example, the $\delta^{18}O_{apatite}$ paleothermometer requires an estimate for the $\delta^{18}O$ of Devonian seawater. Joachimski et al. (2009) estimated this value at -1‰ V-SMOW, as the Devonian is considered a non-glaciated time interval. However, only a 0.5‰ higher or lower $\delta^{18}O$ value for the Devonian seawater in which the apatite-bearing conodonts lived, would result in a 2.2°C respective increase or decrease of the $\delta^{18}O_{apatite}$ paleotemperature estimates. A 0.5‰ deviation from the -1‰ VSMOW $\delta^{18}O_{water}$ that is used for calculating paleotempertures is still a conservative estimate, as the oxygen isotope composition of the surface waters in epeiric seas can be strongly influenced by evaporation or freshwater input. The comparison between the variation in $\delta^{18}O_{apatite}$ and the variation in our simulations is not affected by the uncertainty on the oxygen isotope composition of Devonian seawater. The simulated temperature variability due to astronomical forcing explains 30 to 60% of the observed variance in isotopic paleotemperatures. Moreover, the variance of the observations is a lower bound estimate of the true climate variance. For example, it is possible that conodont-bearing animals thrived better under warmer climates so that the $\delta^{18}O_{apatite}$ samples are biased towards the higher temperature estimates and thus only represent part of the true range. Consequently, the model almost certainly underestimates the actual Devonian climate variability. This discrepancy may be induced by missing feedbacks (e.g. vegetation or pCO_2 response to astronomical forcing changes), or by drivers of Late Devonian climate variability other than the astronomical forcing, be they internal or external.

5.3. Implications for cyclostratigraphic studies

Cyclic alternations between limestones, shales and marls in the Holy Cross Mountains, Poland were earlier interpreted as eccentricity cycles (De Vleeschouwer et al., 2013). Our climate model simulations contribute to better understand the role astronomical climate forcing played in the triggering and/or pacing of these events. To this end, we create a 10-Myr long time-series of the mean annual temperature at the paleolocation of Poland (eastern Euramerica). Figure 16b shows that under moderate forcing, the mean annual temperature at the paleolocation of Poland is around 29.5°C. However, more extreme astronomical configurations exist under which the mean annual temperature goes up to 32.5°C. These exceptionally warm climates occur when eccentricity and obliquity reach simultaneous maxima. Because of the combined effect of eccentricity and obliquity, the amount of time separating the exceptionally warm climates is not regular. This also explains why the periods of significant warming do not exactly align with the 405-kyr eccentricity maxima. In De Vleeschouwer et al. (2013), the results of wavelet and spectral analyses lead to the hypothesis that a connection exists between ocean anoxia and exceptionally high eccentricity. This hypothesis is further developed here. We compare the Upper Kellwasser Event (UKE) $\delta^{18}O_{carb}$ record from the Kowala section, containing the Frasnian-Famennian boundary, with a simulated exceptionally warm climate at the paleolocation of Poland. The cyclostratigraphic framework for this $\delta^{18}O_{carb}$ record suggests that this 16.05 m interval corresponds to 780 kyr

(Fig. 3 in De Vleeschouwer et al., 2013). No circular reasoning is involved here, as the cyclostratigraphic framework for this section is constructed based on the limestone/shale alternations, and thus not on the basis of the $\delta^{18}O_{carb}$ record itself. Hence, we calculate the Pearson correlation coefficient for each possible alignment of a 780-kyr long simulated temperature series with the $\delta^{18}O_{carb}$ record. The correlation between data and model is optimal (r=-0.51), when the simulated temperature series between -3.4 and -2.62 Myr is aligned with the $\delta^{18}O_{carb}$ record. This specific correlation coefficient largely exceeds the 99% confidence level (CL) for red noise (r=-0.31). This means such a good fit is highly unlikely to be obtained by correlating the $\delta^{18}O_{carb}$ record with red noise that has the same probability density function than the astronomically-forced time series that is shown in Fig. 16b. In this specific alignment, the largest negative isotope excursion corresponds to an extremely-high mean annual temperature in Poland of 31.8°C (Figs. 16c and 16d). Moreover, this alignment causes different negative and positive excursions in the UKE isotope record to correspond with respectively maxima and minima in the simulated temperature record (dashed lines on Fig. 16d). These results suggest that astronomical climate forcing played an important role as the trigger of Late Devonian anoxic events. Also the timing of hot and cold pulses during the event seems modulated by astronomical forcing. The large variation in $\delta^{18}O_{carb}$ (>2‰) suggests temperature variations of about 8°C, if the effects of salinity and ice volume changes are neglected. This value is twice as large as the temperature variations that are simulated for the paleolocation of Poland (Figs. 16b,d). This discrepancy is possibly due to climate feedback mechanisms related to the global carbon cycle that are not included into the model. These undoubtedly played a significant role in amplifying the climatic changes during the UKE period of anoxic shale formation. Changes in ice volume might be a secondary factor in the explanation of the large $\delta^{18}O_{carb}$ amplitude.

6. Conclusions

The different simulated climates demonstrate the significant and influential role of eccentricity, obliquity and precession on the Late Devonian greenhouse climate. The highest simulated global mean temperature is 27°C, reached under simultaneous high obliquity, high eccentricity and $\tilde{\omega} = 180°$. This is as much as 8°C warmer than the coolest simulated global climate, under low obliquity and a circular orbit. A comparison of the simulated "median orbit" climate with geological indicators of paleoclimate and results from $\delta^{18}O_{apatite}$ paleothermometry demonstrates that HadSM3 succeeds in simulating meaningful Late Devonian climates. Moreover, the application of the HadSM3 model to Late Devonian boundary conditions provides insight into the mechanisms (albedo feedback and tropical dynamics) determining the greenhouse climate sensitivity to astronomical forcing. However, the results in this study only represent a first-order estimate of the Late Devonian climate response to astronomical forcing: Large uncertainties exist on the boundary conditions that are used to run the model and several potential feedback mechanisms are not taken into account by the model. Still, our first-order estimates prove useful to obtain a more thorough understanding of cyclic changes within the stratigraphic column of the Late Devonian. The comparison of a high-resolution $\delta^{18}O_{carb}$ record across the Upper Kellwasser event with the model's climate simulations suggests the important steering role of astronomical forcing in triggering and pacing Late Devonian anoxic events.

7. Acknowledgements

This work is supported by a Ph.D. fellowship awarded by the Research Foundation – Flanders (FWO) assigned to DDV. MC is research associate with the Belgian National Fund of Scientific Research. Computational resources have been provided by the supercomputing facilities of the Université catholique de Louvain (CISM/UCL). MC and NB are supported by the EU FP7 ERC Starting Grant nr 239604 "ITOP". PC thanks FWO (G.A078.11), Hercules Foundation and VUB research funds for their contribution.

8. References

Alexeev, V.A., Langen, P.L. and Bates, J.R., 2005. Polar amplification of surface warming on an aquaplanet in "ghost forcing" experiments without sea ice feedbacks. Climate Dynamics, 24(7-8), 655-666.

Algeo, T.J. and Scheckler, S.E., 1998. Terrestrial-marine teleconnections in the Devonian: links between the evolution of land plants, weathering processes, and marine anoxic events. Philosophical Transactions of the Royal Society B-Biological Sciences, 353(1365), 113-128.

Bai, S.L., 1995. Milankovitch Cyclicity and Time Scale of the Middle and Upper Devonian. International Geology Review, 37(12), 1109-1114.

Becker, R.T., Gradstein, F.M. and Hammer, O., 2012. The Devonian Period. In: F.M. Gradstein, J.G. Ogg, M.D. Schmitz and G. Ogg (Eds.), The Geologic Time Scale 2012. Elsevier, Amsterdam, pp. 559-601.

Bell, C.J., Gray, L.J. and Kettleborough, J., 2010. Changes in Northern Hemisphere stratospheric variability under increased CO2 concentrations. Quarterly Journal of the Royal Meteorological Society, 136(650), 1181-1190.

Berger, A., Loutre, M.F. and Laskar, J., 1992. Stability of the Astronomical Frequencies over the Earth's History for Paleoclimate Studies. Science, 255, 560-565.

Berner, R.A., 2006. GEOCARBSULF: A combined model for Phanerozoic atmospheric O-2 and CO2. Geochimica et Cosmochimica Acta, 70(23), 5653-5664.

Betts, R.A., Boucher, O., Collins, M., Cox, P.M., Falloon, P.D., Gedney, N., Hemming, D.L., Huntingford, C., Jones, C.D., Sexton, D.M.H. and Webb, M.J., 2007. Projected increase in continental runoff due to plant responses to increasing carbon dioxide. Nature, 448(7157), 1037-U5.

Bijl, P.K., Schouten, S., Sluijs, A., Reichart, G.-J., Zachos, J.C. and Brinkhuis, H., 2009. Early Palaeogene temperature evolution of the southwest Pacific Ocean. Nature, 461(7265), 776-779.

Blakey, R., 2010. Global Paleogeography. http://www2.nau.edu/rcb7/globaltext2.html. Last Accessed on: 22/02/2011

Brayshaw, D.J., Rambeau, C.M.C. and Smith, S.J., 2011. Changes in Mediterranean climate during the Holocene: Insights from global and regional climate modelling. Holocene, 21(1), 15-31.

Caputo, M.V., de Melo, J.H.G., Streel, M. and Isbell, J.L., 2008. Late Devonian and Early Carboniferous glacial records of South America. Resolving the Late Paleozoic Ice Age in Time and Space, 441, 161-173.

Chen, D.Z. and Tucker, M.E., 2003. The Frasnian-Famennian mass extinction: insights from high-resolution sequence stratigraphy and cyclostratigraphy in South China. Palaeogeography Palaeoclimatology Palaeoecology, 193(1), 87-111.

Chlupáč, I., 2000. Cyclicity and duration of Lower Devonian stages: Observations from the Barrandian area, Czech Republic. Neues Jahrbuch Fur Geologie Und Palaontologie-Abhandlungen, 215(1), 97-124.

Cofiño, A.S., Cano, R., Sordo, C., Primo, C. and Gutiérrez, J.M., 2004. MeteoLab, a software library for Matlab>= 5 implementing statistical and data mining techniques for Meteorology. Applied Meteorology Group. Universidad de Cantabria.

Collins, M., Booth, B.B.B., Harris, G.R., Murphy, J.M., Sexton, D.M.H. and Webb, M.J., 2006. Towards quantifying uncertainty in transient climate change. Climate Dynamics, 27(2-3), 127-147.

Copper, P., 2002. Silurian and Devonian reefs: 80 million years of global greenhouse between two ice ages. Society of Economic Paleontologists and Mineralogists Special Publication, 72, 181-238.

Cox, P.M., Betts, R.A., Bunton, C.B., Essery, R.L.H., Rowntree, P.R. and Smith, J., 1999. The impact of new land surface physics on the GCM simulation of climate and climate sensitivity. Climate Dynamics, 15(3), 183-203.

Craggs, H.J., Valdes, P.J. and Widdowson, M., 2012. Climate model predictions for the latest Cretaceous: An evaluation using climatically sensitive sediments as proxy indicators. Palaeogeography Palaeoclimatology Palaeoecology, 315, 12-23.

Cressler, W.L., Daeschler, E.B., Slingerland, R. and Peterson, D.A., 2010. Terrestrialization in the Late Devonian: a palaeoecological overview of the Red Hill site, Pennsylvania, USA. In: M. Vecoli,

G. Clément and B. Meyer-Berthaud (Eds.), The Terrestrialization Process: Modelling Complex Interactions at the Biosphere-Geosphere Interface. Geol. Soc. SP., London, pp. 111-128.

Crick, R.E., Ellwood, B.B., Hladil, J., El Hassani, A., Hrouda, F. and Chlupac, I., 2001. Magnetostratigraphy susceptibility of the Pridolian-Lochkovian (Silurian-Devonian) GSSP (Klonk, Czech Republic) and a coeval sequence in Anti-Atlas Morocco. Paleogeography, Paleoclimatology, Palaeoecology, 167, 73-100.

Crucifix, M., Betts, R.A. and Cox, P.M., 2005. Vegetation and climate variability: a GCM modelling study. Climate Dynamics, 24(5), 457-467.

Crucifix, M. and Hewitt, C.D., 2005. Impact of vegetation changes on the dynamics of the atmosphere at the Last Glacial Maximum. Climate Dynamics, 25(5), 447-459.

De Vleeschouwer, D., Da Silva, A.C., Boulvain, F., Crucifix, M. and Claeys, P., 2012a. Precessional and half-precessional climate forcing of Mid-Devonian monsoon-like dynamics. Climate of the Past, 8(1), 337-351.

De Vleeschouwer, D., Whalen, M.T., Day, J.E. and Claeys, P., 2012b. Cyclostratigraphic calibration of the Frasnian (Late Devonian) time scale (western Alberta, Canada). Geological Society of America Bulletin, 124(5-6), 928-942.

De Vleeschouwer, D., Rakociński, M., Racki, G., Bond, D.P.G., Sobień, K. and Claeys, P., 2013. The astronomical rhythm of Late-Devonian climate change (Kowala section, Holy Cross Mountains, Poland). Earth and Planetary Science Letters, 365, 25-37.

Dunagan, S.P. and Driese, S.G., 1999. Control of terrestrial stabilization on Late Devonian palustrine carbonate deposition: Catskill Magnafacies, New York, USA. Journal of Sedimentary Research, 69(3), 772-783.

Ellwood, B.B., Algeo, T.J., El Hassani, A., Tomkin, J.H. and Rowe, H.D., 2011a. Defining the timing and duration of the Kacak Interval within the Eifelian/Givetian boundary GSSP, Mech Irdane, Morocco, using geochemical and magnetic susceptibility patterns. Palaeogeography Palaeoclimatology Palaeoecology, 304(1-2), 74-84.

Ellwood, B.B., Tomkin, J.H., El Hassani, A., Bultynck, P., Brett, C.E., Schindler, E., Feist, R. and Bartholomew, A., 2011b. A climate-driven model and development of a floating point time scale for the entire Middle Devonian Givetian Stage: A test using magnetostratigraphic susceptibility as a climate proxy. Palaeogeography Palaeoclimatology Palaeoecology, 304(1-2), 85-95.

Embry, A.F. and Klovan, J.E., 1972. Absolute water depth limits of Late Devonian paleoecological zones. Geologische Rundschau, 61(2), 672-686.

Godderis, Y., Donnadieu, Y., Le Hir, G., Lefebvre, V. and Nardin, E., 2014. The role of palaeogeography in the Phanerozoic history of atmospheric CO2 and climate. Earth-Science Reviews, 128, 122-138.

Gough, D.O., 1981. Solar interior structure and luminosity variations. Solar Physics, 74(1), 21-34.

Han, D.X., 1989. The Features of Devonian Coal-Bearing Deposits in South China, the Peoples-Republic-of-China. International Journal of Coal Geology, 12(1-4), 209-223.

Haywood, A.M., Valdes, P.J. and Sellwood, B.W., 2002. Magnitude of climate variability during middle Pliocene warmth: a palaeoclimate modelling study. Palaeogeography Palaeoclimatology Palaeoecology, 188(1-2), 1-24.

Heckel, P.H. and Witzke, B.J., 1979. Devonian world paleogeography determined from distribution of carbonates and related lithic paleoclimatic indicators. In: M.R. House, C.T. Scrutton and M.G. Bassett (Eds.), The Devonian System. Spec. Pap. Palaeontol., London, pp. 99-123.

Holland, M.M. and Bitz, C.M., 2003. Polar amplification of climate change in coupled models. Climate Dynamics, 21(3-4), 221-232.

House, M.R., 1991. Devonian sedimentary microrhythms and a Givetian time scale. Proceedings of the Ussher Society, 7, 392-395.

House, M.R., 1995. Devonian precessional and other signatures for establishing a Givetian timescale. In: M.R. House and A.S. Gale (Eds.), Orbital forcing timescales and cyclostratigraphy. Geological Society of London, Special Publications, London, pp. 37-49.

Hurley, N.F. and Van der Voo, R., 1987. Paleomagnetism of Upper Devonian Reefal Limestones, Canning Basin, Western-Australia. Geological Society of America Bulletin, 98(2), 138-146.

Isaacson, P.E., Diaz-Martinez, E., Grader, G.W., Kalvoda, J., Babek, O. and Devuyst, F.X., 2008. Late Devonian-earliest Mississippian glaciation in Gondwanaland and its biogeographic consequences. Palaeogeography Palaeoclimatology Palaeoecology, 268(3-4), 126-142.

Isbell, J.L., Miller, M.F., Wolfe, K.L. and Lenaker, P.A., 2003. Timing of late Paleozoic glaciation in Gondwana: Was glaciation responsible for the development of Northern Hemisphere cyclothems? Geological Society of America Special Papers, 5-24.

Joachimski, M.M., Breisig, S., Buggisch, W., Talent, J.A., Mawson, R., Gereke, M., Morrow, J.R., Day, J. and Weddige, K., 2009. Devonian climate and reef evolution: Insights from oxygen isotopes in apatite. Earth and Planetary Science Letters, 284(3-4), 599-609.

Kim, J.H., Brown, S.J. and McDonald, R.E., 2011. Future changes in tropical cyclone genesis in fully dynamic ocean- and mixed layer ocean-coupled climate models: a low-resolution model study. Climate Dynamics, 37(3-4), 737-758.

Kolodny, Y., Luz, B. and Navon, O., 1983. Oxygen Isotope Variations in Phosphate of Biogenic Apatites .1. Fish Bone Apatite - Rechecking the Rules of the Game. Earth and Planetary Science Letters, 64(3), 398-404.

Laskar, J., Robutel, P., Joutel, F., Gastineau, M., Correia, A.C.M. and Levrard, B., 2004. A long-term numerical solution for the insolation quantities of the Earth. Astronomy & Astrophysics, 428, 261-285.

Laskar, J., Fienga, A., Gastineau, M. and Manche, H., 2011. La2010: a new orbital solution for the long-term motion of the Earth. Astronomy & Astrophysics, 532.

Le Hir, G., Donnadieu, Y., Goddéris, Y., Meyer-Berthaud, B., Ramstein, G. and Blakey, R.C., 2011. The climate change caused by the land plant invasion in the Devonian. Earth and Planetary Science Letters, 310(3-4), 203-212.

Littler, K., Robinson, S.A., Bown, P.R., Nederbragt, A.J. and Pancost, R.D., 2011. High sea-surface temperatures during the Early Cretaceous Epoch. Nature Geosci, 4(3), 169-172.

MacNeil, A.J. and Jones, B., 2006. Palustrine deposits on a late devonian coastal plain - Sedimentary attributes and implications for concepts of carbonate sequence stratigraphy. Journal of Sedimentary Research, 76(1-2), 292-309.

McGhee, G.R., 1996. The Late Devonian mass extinction: the Frasnian/Famennian crisis. Columbia University Press, New York, 378 pp.

Meyerhof, A.A., 1970. Continental Drift . Implications of Paleomagnetic Studies, Meteorology, Physical Oceanography, and Climatology. Journal of Geology, 78(1), 1-51.

Mordberg, L.E., 1996. Geochemistry of trace elements in Paleozoic bauxite profiles in northern Russia. Journal of Geochemical Exploration, 57(1-3), 187-199.

Otto-Bliesner, B.L., 1993. Tropical mountains and coal formation: A climate model study of the Westphalian (306 Ma). Geophysical Research Letters, 20(18), 1947-1950.

Otto-Bliesner, B.L., 2003. The role of mountains, polar ice, and vegetation in determining the tropical climate during the Middle Pennsylvanian: Climate model simulations. In: C.B. Cecil and N.T. Edgar (Eds.), Climate Controls of Stratigraphy. SEPM Special Publication, pp. 227-237.

Peyser, C.E. and Poulsen, C.J., 2008. Controls on Permo-Carboniferous precipitation over tropical Pangaea: A GCM sensitivity study. Palaeogeography, Palaeoclimatology, Palaeoecology, 268(3), 181-192.

Pope, V.D., Gallani, M.L., Rowntree, P.R. and Stratton, R.A., 2000. The impact of new physical parametrizations in the Hadley Centre climate model: HadAM3. Climate Dynamics, 16(2-3), 123-146.

Scheckler, S.E., 1986. Geology, floristics, and paleoecology of Late Devonian coal swamps from Appalachian Laurentia (USA). Annales de la Société Géologique de Belgique, 109, 209-222.

Scotese, C.R. and Barrett, S.F., 1990. Gondwana's movement over the South Pole during the Palaeozoic: evidence from lithological indicators of climate. In: W.S. McKerrow and C.R. Scotese (Eds.), Palaeozoic palaeogeography and biogeography. Geological Society of London Memoirs. Geological Society of London, pp. 75-86.

Scotese, C.R., 2004. A continental drift flipbook. Journal of Geology, 112(6), 729-741.

Spicer, R.A., Ahlberg, A., Herman, A.B., Hofmann, C.C., Raikevich, M., Valdes, P.J. and Markwick, P.J., 2008. The Late Cretaceous continental interior of Siberia: A challenge for climate models. Earth and Planetary Science Letters, 267(1-2), 228-235.

Stainforth, D.A., Aina, T., Christensen, C., Collins, M., Faull, N., Frame, D.J., Kettleborough, J.A., Knight, S., Martin, A., Murphy, J.M., Piani, C., Sexton, D., Smith, L.A., Spicer, R.A., Thorpe, A.J. and Allen, M.R., 2005. Uncertainty in predictions of the climate response to rising levels of greenhouse gases. Nature, 433(7024), 403-406.

Streel, M., Caputo, M.V., Loboziak, S. and Melo, J.H.G., 2000. Late Frasnian-Famennian climates based on palynomorph analyses and the question of the Late Devonian glaciations. Earth-Science Reviews, 52, 121-173.

Tindall, J., Flecker, R., Valdes, P., Schmidt, D.N., Markwick, P. and Harris, J., 2010. Modelling the oxygen isotope distribution of ancient seawater using a coupled ocean-atmosphere GCM: Implications for reconstructing early Eocene climate. Earth and Planetary Science Letters, 292(3-4), 265-273.

Torsvik, T.H., Van der Voo, R., Preeden, U., Mac Niocaill, C., Steinberger, B., Doubrovine, P.V., van Hinsbergen, D.J.J., Domeier, M., Gaina, C., Tohver, E., Meert, J.G., McCausland, P.J.A. and Cocks, L.R.M., 2012. Phanerozoic polar wander, palaeogeography and dynamics. Earth-Science Reviews, 114(3-4), 325-368.

Turner, A., Sperber, K., Slingo, J., Meehl, G., Mechoso, C., Kimoto, M. and Giannini, A., 2008. Modelling Monsoons: Understanding and Predicting Current and Future Behaviour. In: C.-P. Chang et al. (Eds.), The Global Monsoon System Research and Forecast. World Scientific Publishing Co., Singapore.

Volkova, I.B., 1994. Nature and Composition of the Devonian Coals of Russia. Energy & Fuels, 8(6), 1489-1493.

Williams, K.D., Senior, C.A. and Mitchell, J.F.B., 2001. Transient climate change in the Hadley Centre models: The role of physical processes. Journal of Climate, 14(12), 2659-2674.

Witzke, B.J., 1990. Palaeoclimates contrains for Palaeozoic palaeolatitudes of Laurentia and Euramerica. In: W.S. McKerrow and C.R. Scotese (Eds.), Palaeozoic Palaeogeography and Biogeography. Geo. Soc. Mem., London, pp. 57-73.

9. Tables

Experiment name	**Obliquity (ε)**	**Eccentricity (e)**	**Precession ($\tilde{\omega}$)**	Comment
xaclb	22	0		"Obliquity minimum"
xaclr	22	0.03	0	
xacle	22	0.07	0	
xacls	22	0.03	90	
xaclf	22	0.07	90	
xaclp	22	0.03	180	
xaclc	22	0.07	180	
xaclq	22	0.03	270	
xacld	22	0.07	270	
xacla	23.5	0		"median orbit"
xaclz	23.5	0.03	0	
xacln	23.5	0.07	0	
xacmd	23.5	0.07	45	
xacma	23.5	0.03	90	
xaclo	23.5	0.07	90	"Perihelion in June"
xacme	23.5	0.07	135	
xaclx	23.5	0.03	180	
xacll	23.5	0.07	180	
xacmb	23.5	0.07	225	
xacly	23.5	0.03	270	
xaclm	23.5	0.07	270	"Perihelion in December"
xacmc	23.5	0.07	315	
xaclg	24.5	0		"Obliquity maximum"
xaclv	24.5	0.03	0	
xaclj	24.5	0.07	0	
xaclw	24.5	0.03	90	
xaclk	24.5	0.07	90	
xaclt	24.5	0.03	180	
xaclh	24.5	0.07	180	
xaclu	24.5	0.03	270	
xacli	24.5	0.07	270	

Table 1: Experimental design.

	$\delta^{18}O_{apatite}$ (V-SMOW)				Model Simulations	
	Average $\delta^{18}O_{apatite}$		Standard Deviation		Mean Temperature	Standard deviation
Germany (N=71)	17.90‰	**30.5°C**	0.49‰	**2.1°C**	**27.6°C**	**0.65°C**
France (N=13)	18.13‰	**29.5°C**	0.45‰	**2.0°C**	**23.2°C**	**0.85°C**
Iowa (N=7)	18.42‰	**28.2°C**	0.22‰	**1.0°C**	**24.2°C**	**0.60°C**

Table 2: Comparison between simulated mean annual temperature and observed ones as deduced by $\delta^{18}O_{apatite}$ paleothermometry (Joachimski et al., 2009) over the paleolocations of Germany, France and Iowa.

10. FIGURE CAPTIONS

Figure 1: **(a)** Late Devonian continental distribution and palaeotopography (after Blakey, 2010). **(b)** Delineation of the different climate types and biomes in the "median orbit" Late Devonian climate. All model simulations are carried out with soil and vegetation parameters that reflect this "median orbit" biome pattern.

Figure 2: Seasonally averaged surface temperature in the "median orbit" Late Devonian climate simulation (ε=23.5°, e=0). **(a)** December-January-February; **(b)** March-April-May; **(c)** June-July-August; **(d)** September-October-November.

Figure 3: **(a)** Model comparison of the latitudinal SST gradient between the "median orbit" Late Devonian (ε=23.5°, e=0) and a pre-industrial simulation (HadSM3, 300 ppm pCO_2, ε=23.4°, e=0.0167, $\tilde{\varpi}$=283°). **(b)** Annual and monthly land surface temperature gradients for the Late Devonian illustrate the strong seasonality in Gondwana.

Figure 4: Schematic representation of the main pressure systems, isobars and wind vectors at the surface for **(a)** DJF and **(b)** JJA in the "median orbit" Late Devonian climate simulation (ε=23.5°, e=0). ITCZ=Intertropical convergence zone; L = low pressure cell; H = high pressure cell; DJF=December-January-February; JJA=June-July-August.

Figure 5: Seasonally averaged precipitation rate in the "median orbit" Late Devonian climate simulation (ε=23.5°, e=0). **(a)** December-January-February; **(b)** March-April-May; **(c)** June-July-August; **(d)** September-October-November.

Figure 6: **(a)** Model comparison of latitudinally averaged precipitation rate between the "median orbit" Late Devonian climate simulation (ε=23.5°, e=0) and a pre-industrial simulation (HadSM3, 300 ppm pCO_2, ε=23.4°, e=0.0167, $\tilde{\varpi}$=283°). **(b)** Annual and monthly precipitation rates in the Late Devonian show a more confined ITCZ in July than in January.

Figure 7: Climatograms from four different monsoonal systems (dark grey dots) and from two tropical climates in northern Euramerica (light grey dots) in the "median orbit" Late Devonian climate simulation (ε=23.5°, e=0).

Figure 8: Seasonal differences in surface temperature (T_s) between perihelion in December and perihelion in June (ε=23.5, e=0.07), i.e. experiment *xaclm* minus experiment *xaclo*. **(a)** December-January-February; **(b)** March-April-May; **(c)** June-July-August; **(d)** September-October-November.

Figure 9: Seasonal differences in precipitation (PP) between perihelion in December and perihelion in June (ε=23.5, e=0.07), i.e. experiment *xaclm* minus experiment *xaclo*. **(a)** December-January-February; **(b)** March-April-May; **(c)** June-July-August; **(d)** September-October-November.

Figure 10: **(a-b)** Net cloud radiative forcing (NetCRF) during DJF, normalized for incoming solar radiation at the top of the atmosphere, for experiments **(a)** *xaclm* and **(b)** *xaclo*. More negative values in *xaclm* indicate that a more dense DJF cloud cover instigates a negative feedback mechanism by increasing planetary albedo. **(c)** The location map shows that the spring snow cover has a larger extent in both space and time in *xaclm*, compared to *xaclo*. For the location indicated by a dot, the monthly differences in incoming solar radiation at the Earth's surface (green line), snow cover (blue line) and surface temperature (purple line) between *xaclm* and *xaclo* are shown. The larger snow cover in *xaclm* instigates an albedo feedback mechanism that causes much lower spring temperatures. DJF=December-January-February; SON=September-October-November.

Figure 11: Seasonal differences in surface temperature (T_s) between two extreme obliquity simulations (e=0), i.e. experiment *xaclg* minus experiment *xaclb*. **(a)** December-January-February; **(b)** March-April-May; **(c)** June-July-August; **(d)** September-October-November.

Figure 12: Seasonal differences in precipitation (PP) between two extreme obliquity simulations (e=0), i.e. experiment *xaclg* minus experiment *xaclb*. **(a)** December-January-February; **(b)** March-April-May; **(c)** June-July-August; **(d)** September-October-November.

Figure 13: Global temperature and precipitation response to astronomical forcing. **(a)** Surface temperature and **(b)** precipitation in function of obliquity and $e \cdot \sin\tilde{\omega}$, and **(c-d)** in function of $e \cdot \sin\tilde{\omega}$ and $e \cdot \cos\tilde{\omega}$. The latter plots can be read as a polar plot, of which the azimuth is

determined by precession and the distance from the pole by eccentricity. The month during which the Earth reaches perihelion is indicated at the corresponding azimuth.

Figure 14: **(a-d)** Annual and **(e-h)** austral summer (DJF) climate simulator response to astronomical forcing in southeastern Euramerica. **(a,e)** Surface temperature and **(b,f)** precipitation in function of obliquity and $e \cdot \sin \tilde{\omega}$, and **(c,d,g,h)** in function of $e \cdot \sin \tilde{\omega}$ and $e \cdot \cos \tilde{\omega}$ (bottom).

Figure 15: The difference between simulated yearly evaporation and precipitation (E-P) and simulated climate types in the "median orbit" Late Devonian simulation. The comparison with lithic indicators of paleoclimate (PALEOMAP project, Scotese and Barrett, 1990; Witzke, 1990) indicates that the model makes a reasonable estimate of the latitudinal extent of the major climate zones..

Figure 16: **(a)** Eccentricity over the last 10 Ma (Laskar et al., 2004). Together with obliquity and precession, the eccentricity series is run through the simulated 3-D regional climate response to astronomical forcing at the paleolocation of Poland to obtain **(b)** a 10-Myr long time series of mean annual temperature (MAT) for this paleolocation. **(c)** Pearson's correlation coefficient between 780-kyr wide MAT windows and the $\delta^{18}O_{carb}$ record. The correlation is optimal when **(d)** the MAT window between -3.4 and -2.62 Myr is aligned with the $\delta^{18}O_{carb}$ record. In this specific alignment, an extremely warm simulated regional climate corresponds to the largest negative $\delta^{18}O_{carb}$ excursion and several isotopic maxima and minima line up with resp. cool and warm regional climates in Poland.

11. Supporting Material

11.1. Appendix 1

Parameter	Topical A-climates	Dry B-climates	Mild mid-latitude C-climates	Severe mid-latitude D-climates	Polar E-climates
Canopy Height (m)	20	0.5	20	10	0.5
Deep Snow albedo	0.23	0.8	0.6	0.6	0.8
Infiltration enhancement factor	5.5	0.5	2	2	0.75
Leaf area index	8	2.5	3.5	3.5	1
Root depth (m)	1.4	0.15	0.7	0.7	0.15
Roughness length (m)	1.05	0.1	0.3	0.3	0.2
Snow free albedo	0.15	0.3	0.2	0.2	0.3
Surface capacity (kg/m^2)	0.75	0.55	0.65	0.65	0.5
Surface Resistance to evaporation (s/m)	128	105	80	80	0
Vegetation fraction	0.95	0.25	0.9	0.8	0.3

Figure01
Click here to download high resolution image

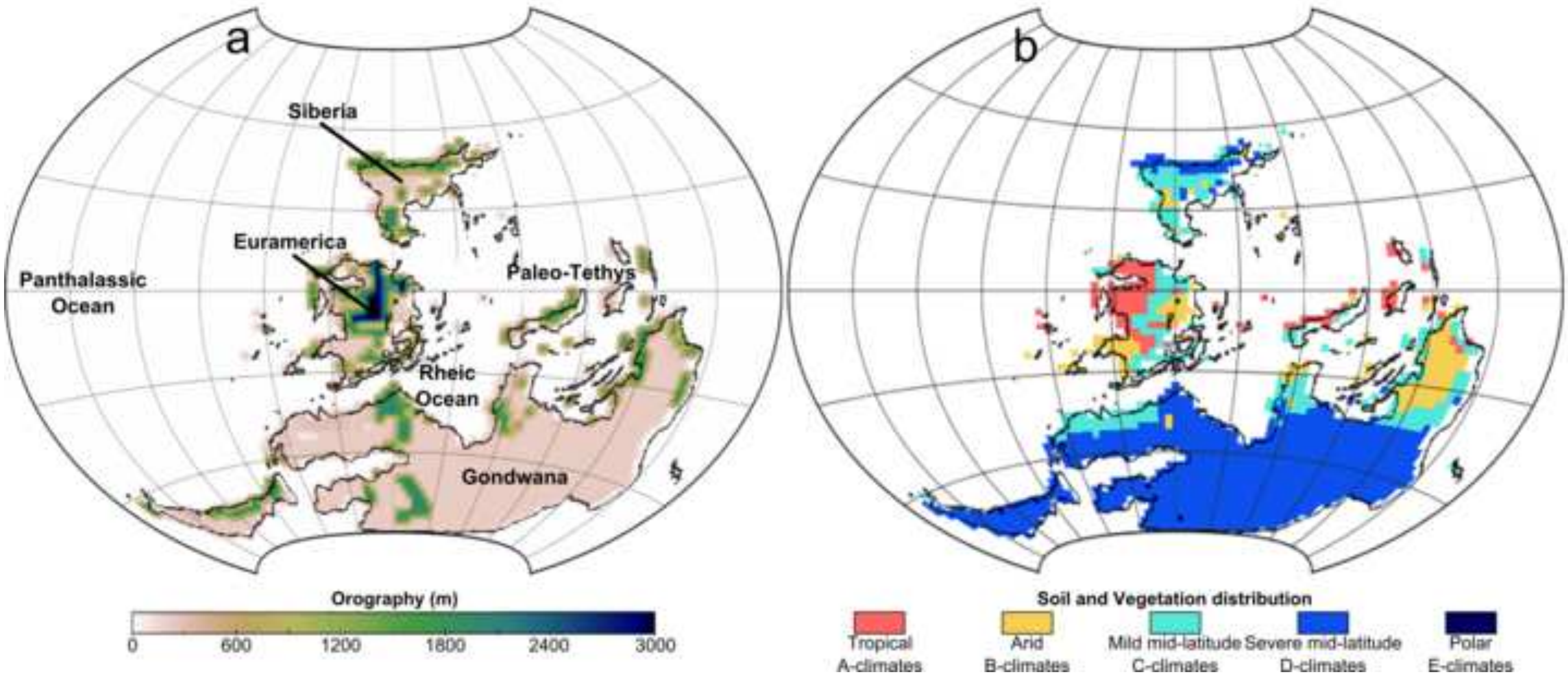

Figure02

Click here to download high resolution image

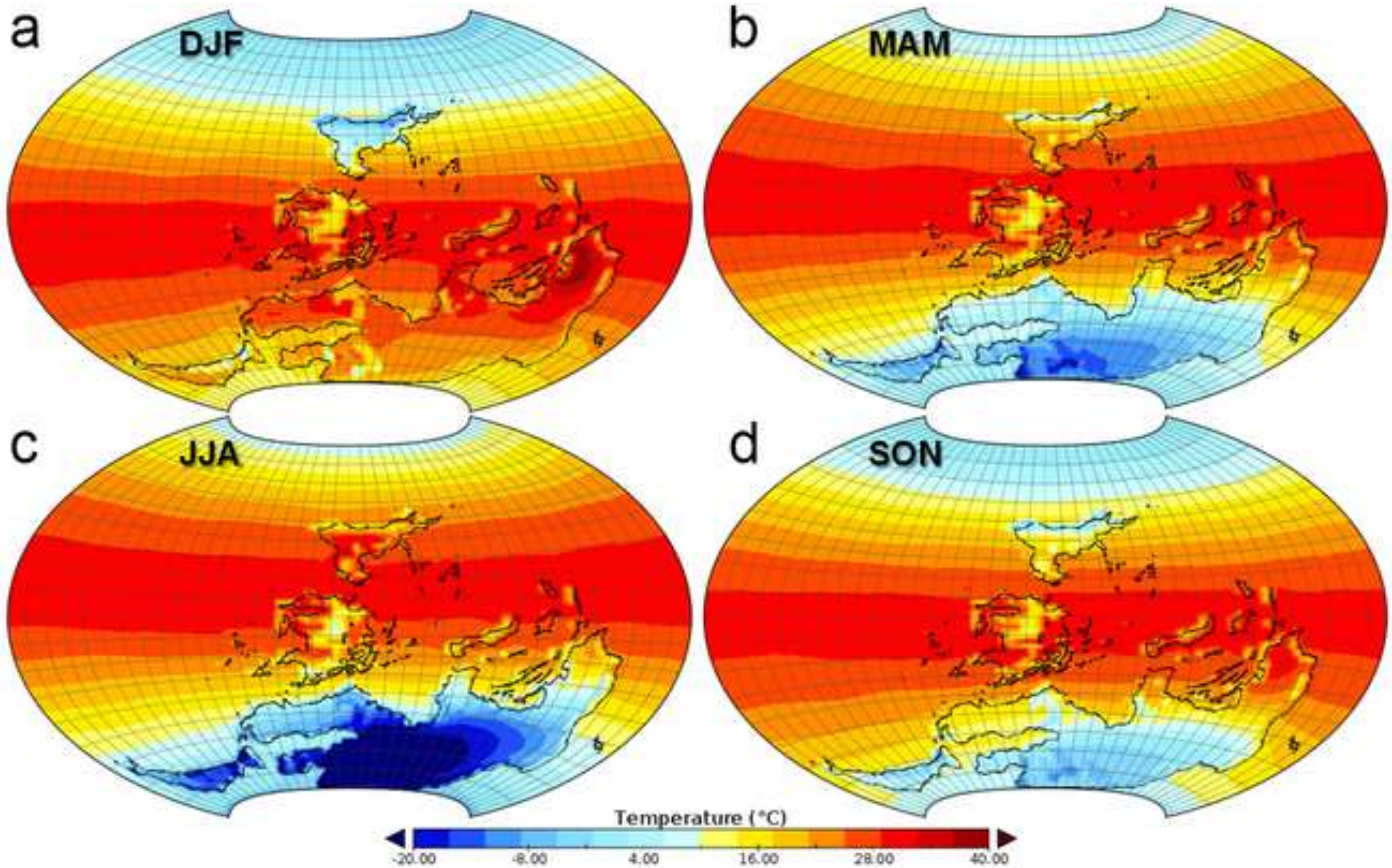

Figure03

Click here to download high resolution image

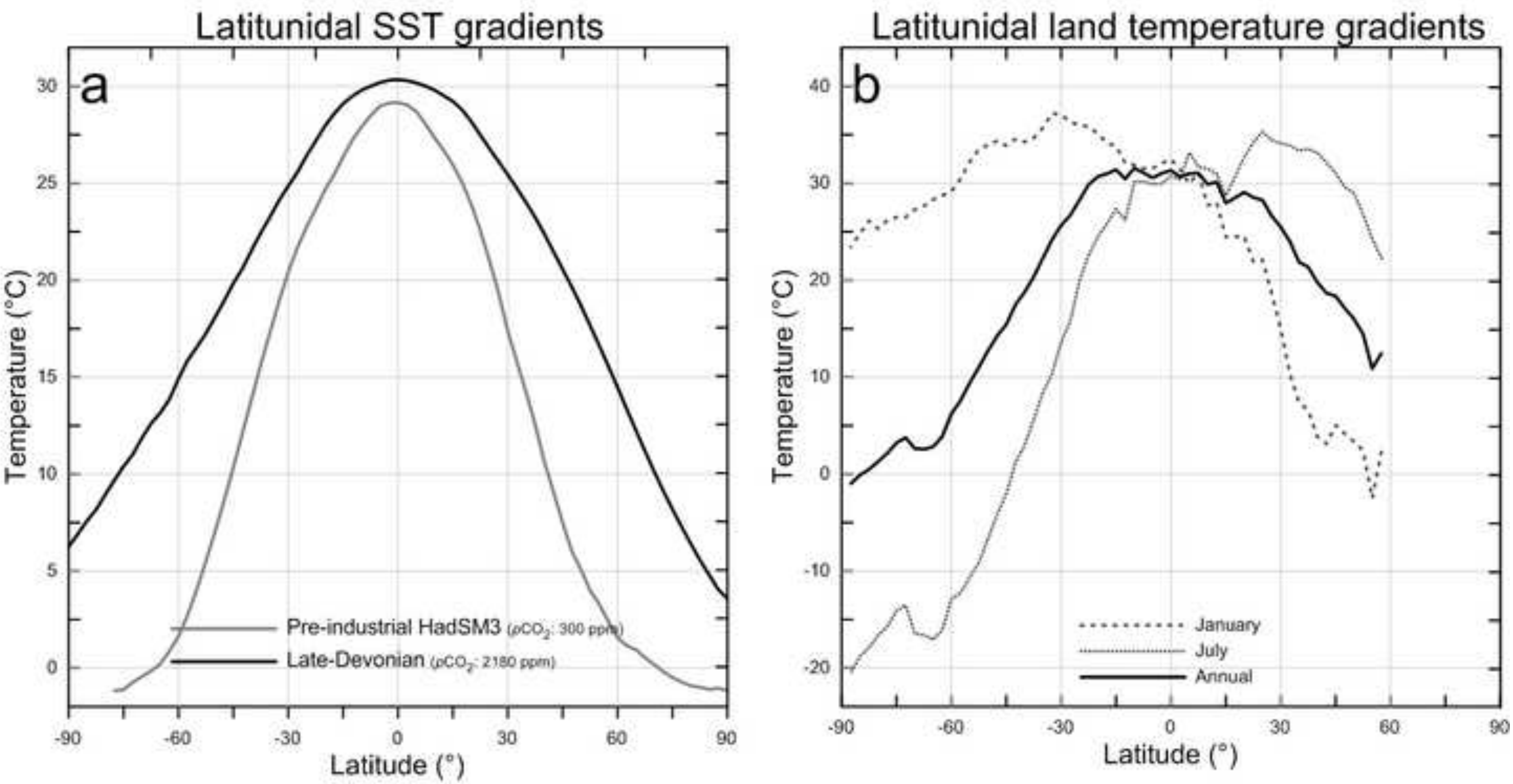

Figure04
Click here to download high resolution image

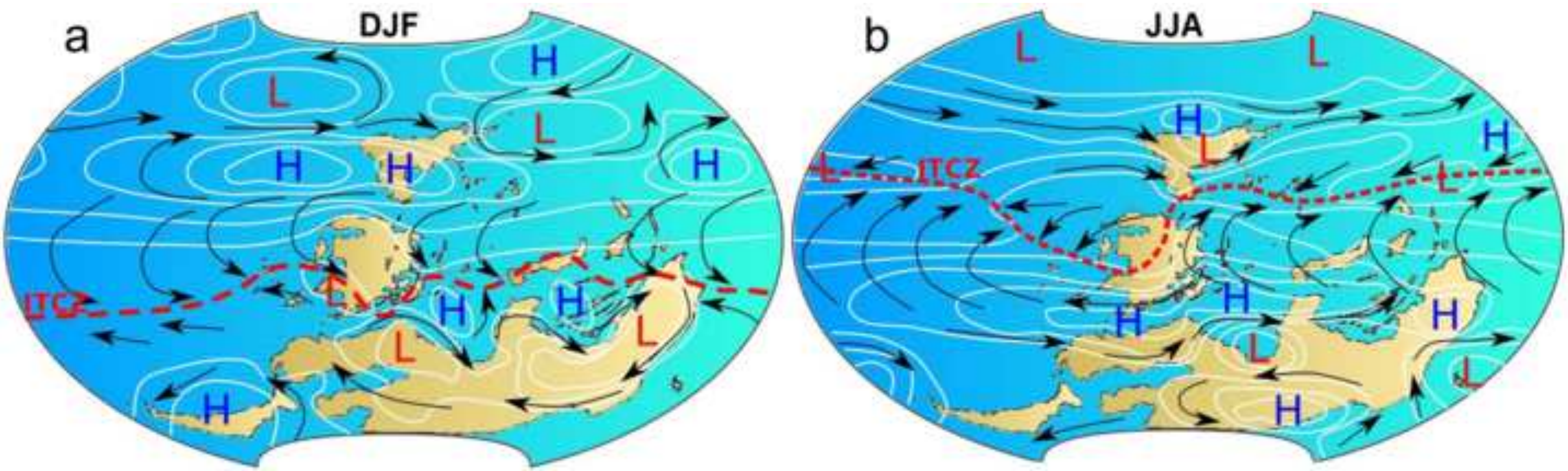

Figure05
Click here to download high resolution image

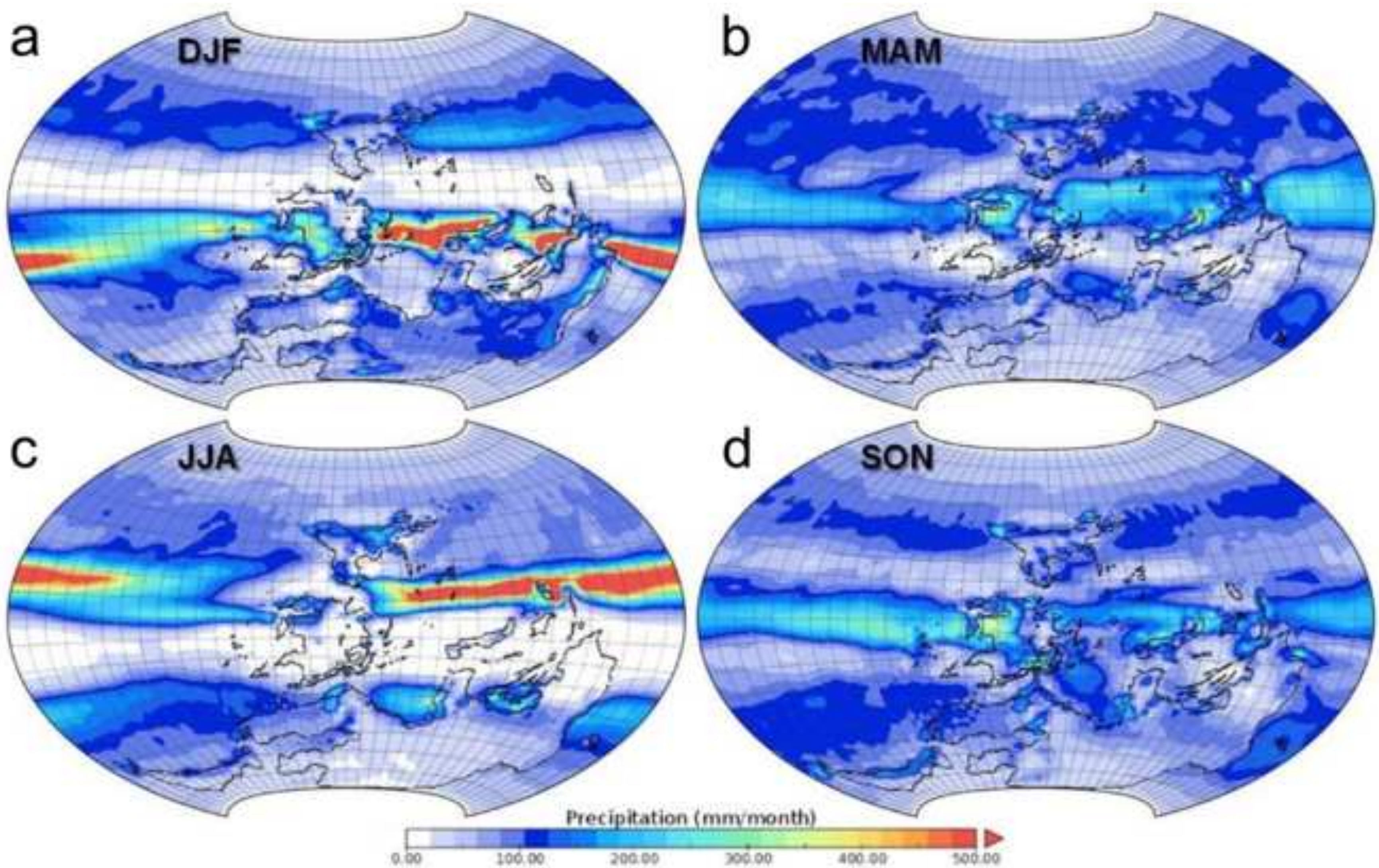

Figure06

Click here to download high resolution image

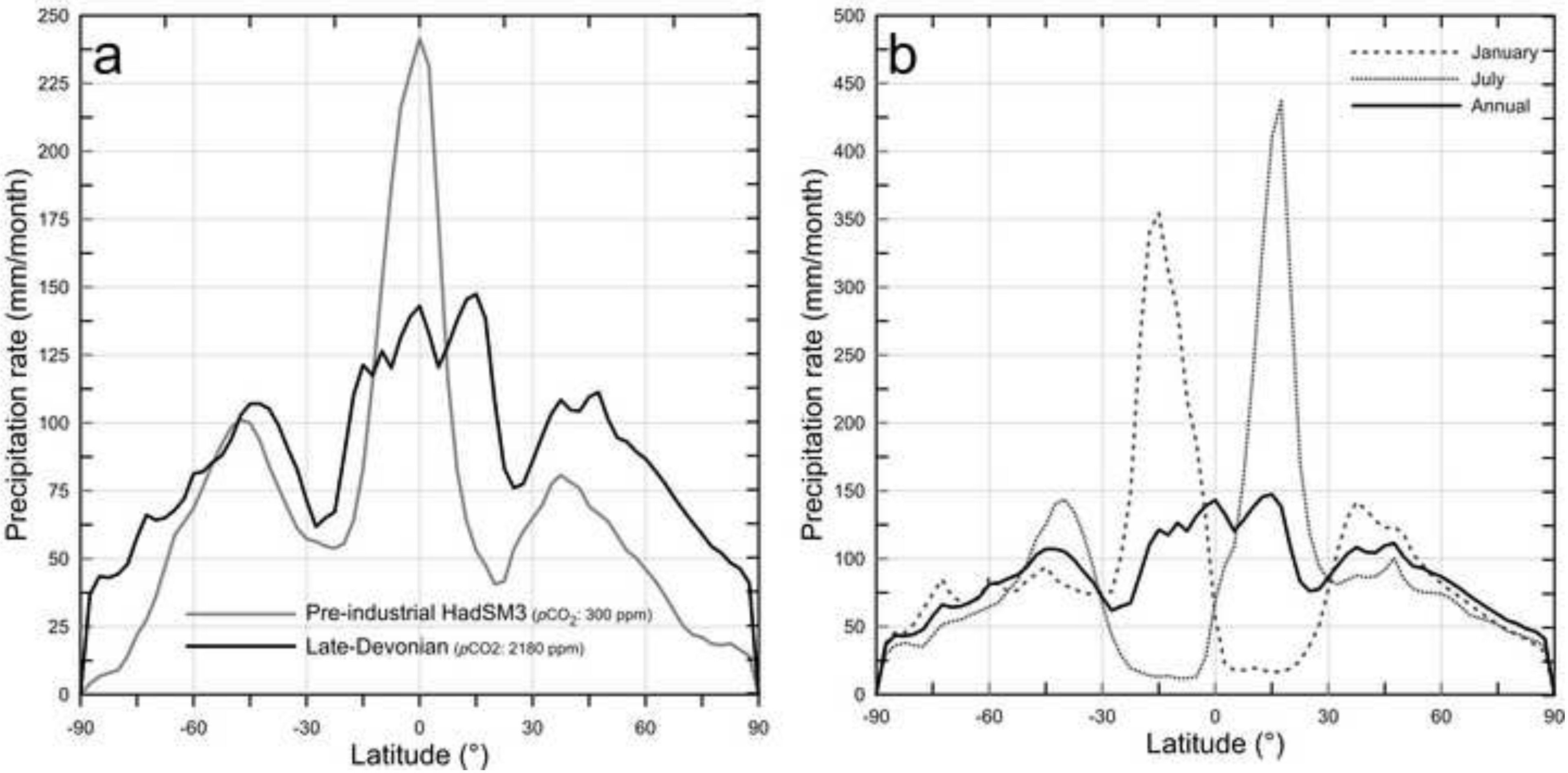

Figure07

Click here to download high resolution image

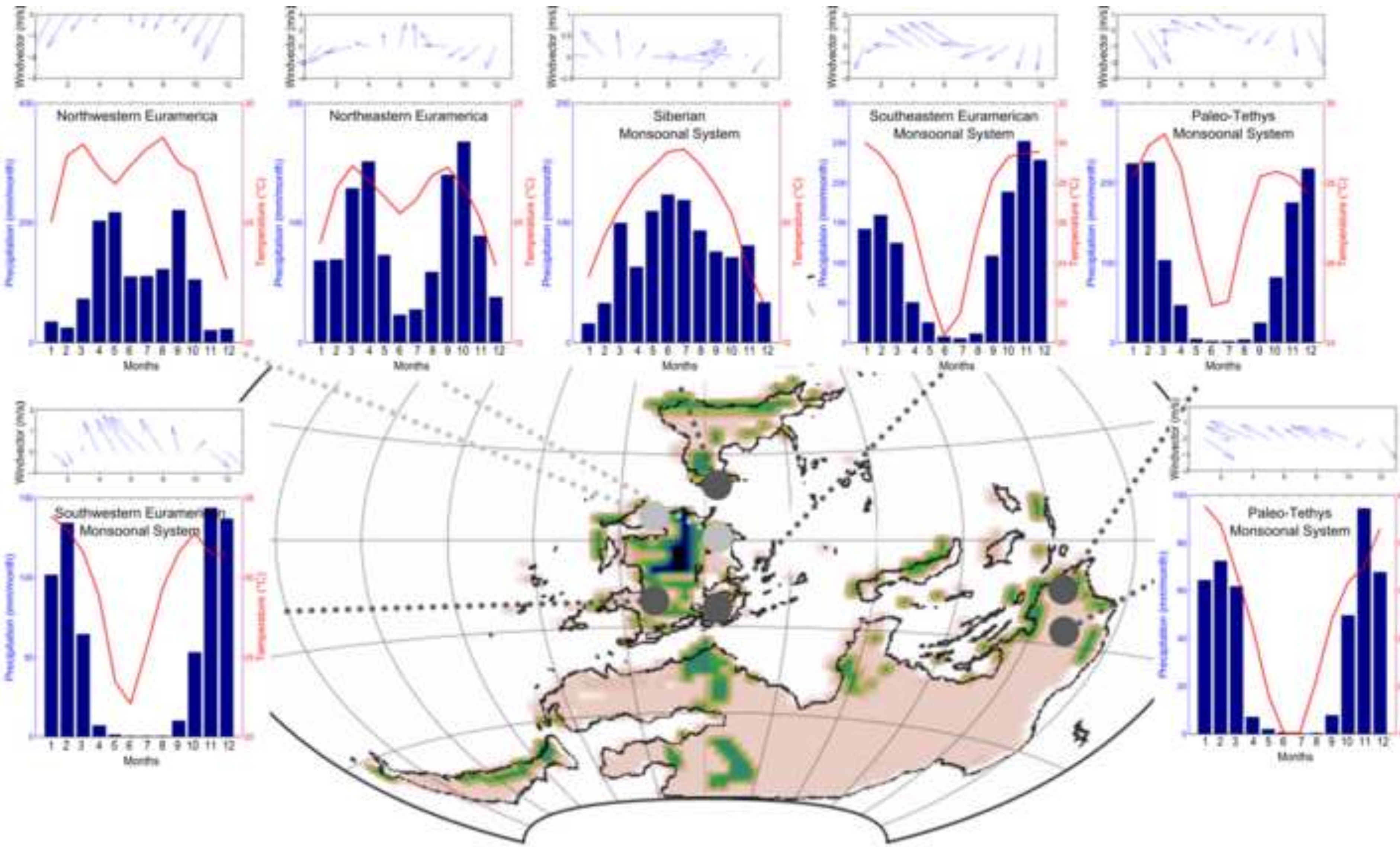

Figure08

Click here to download high resolution image

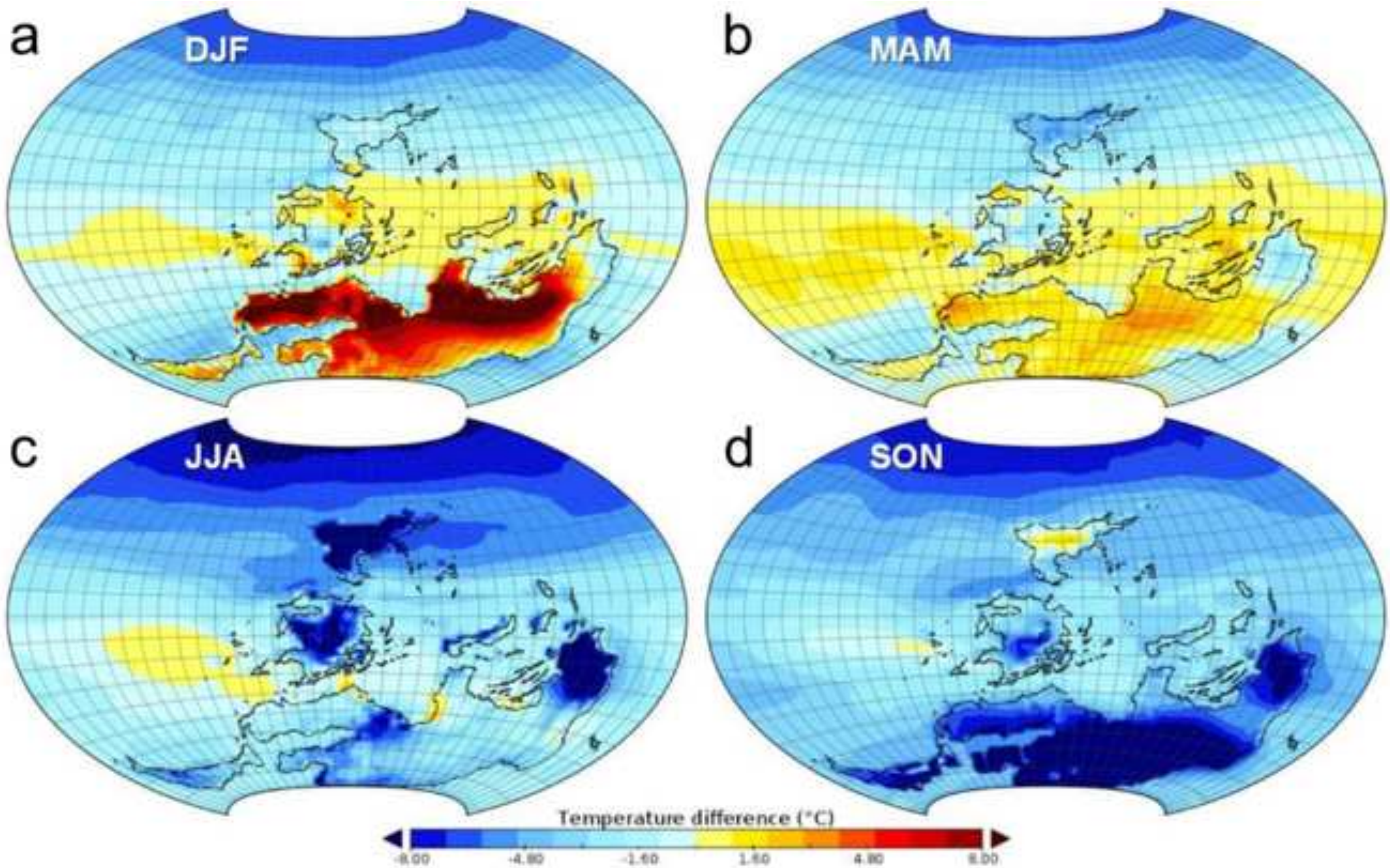

Figure09
Click here to download high resolution image

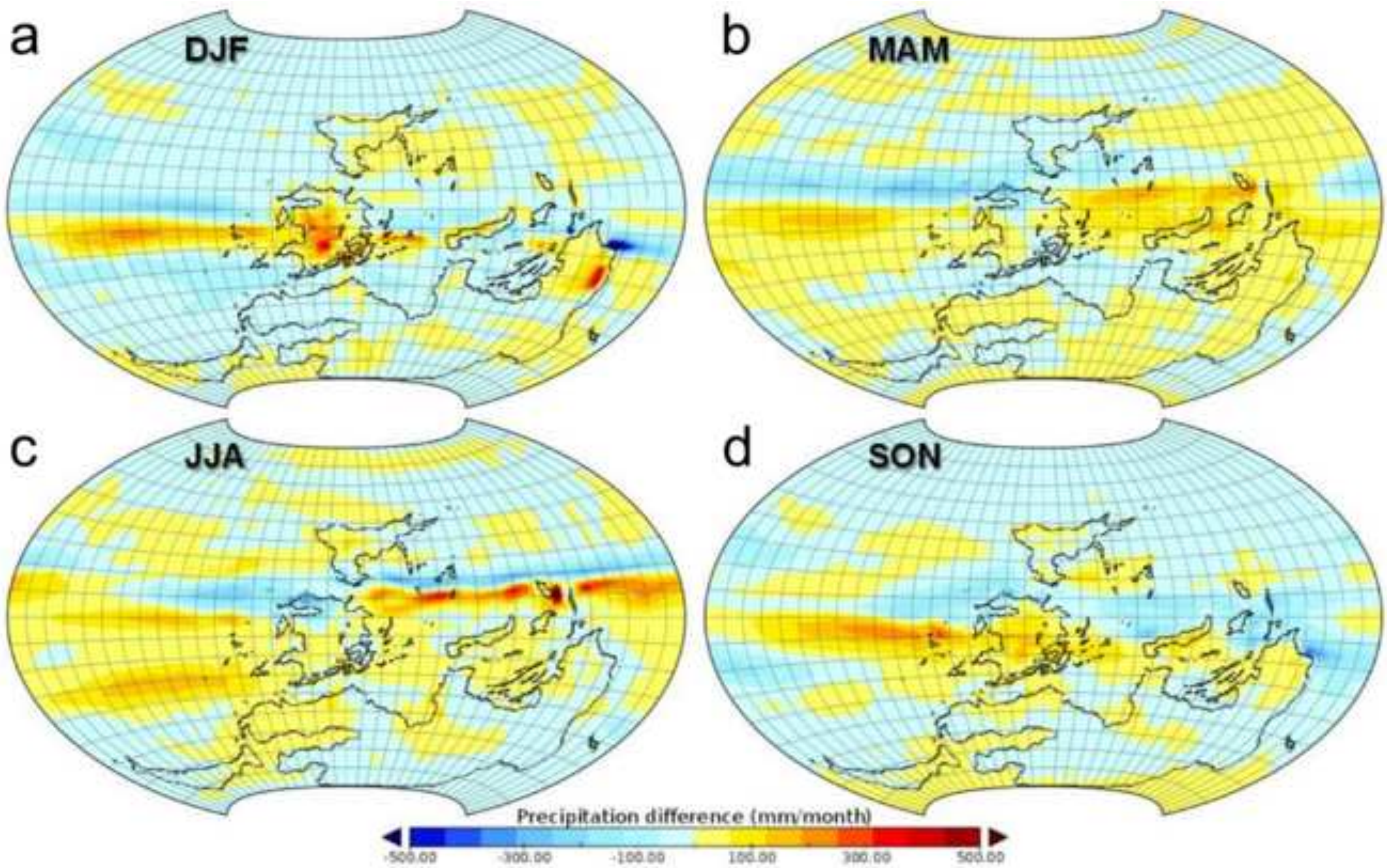

Figure10
Click here to download high resolution image

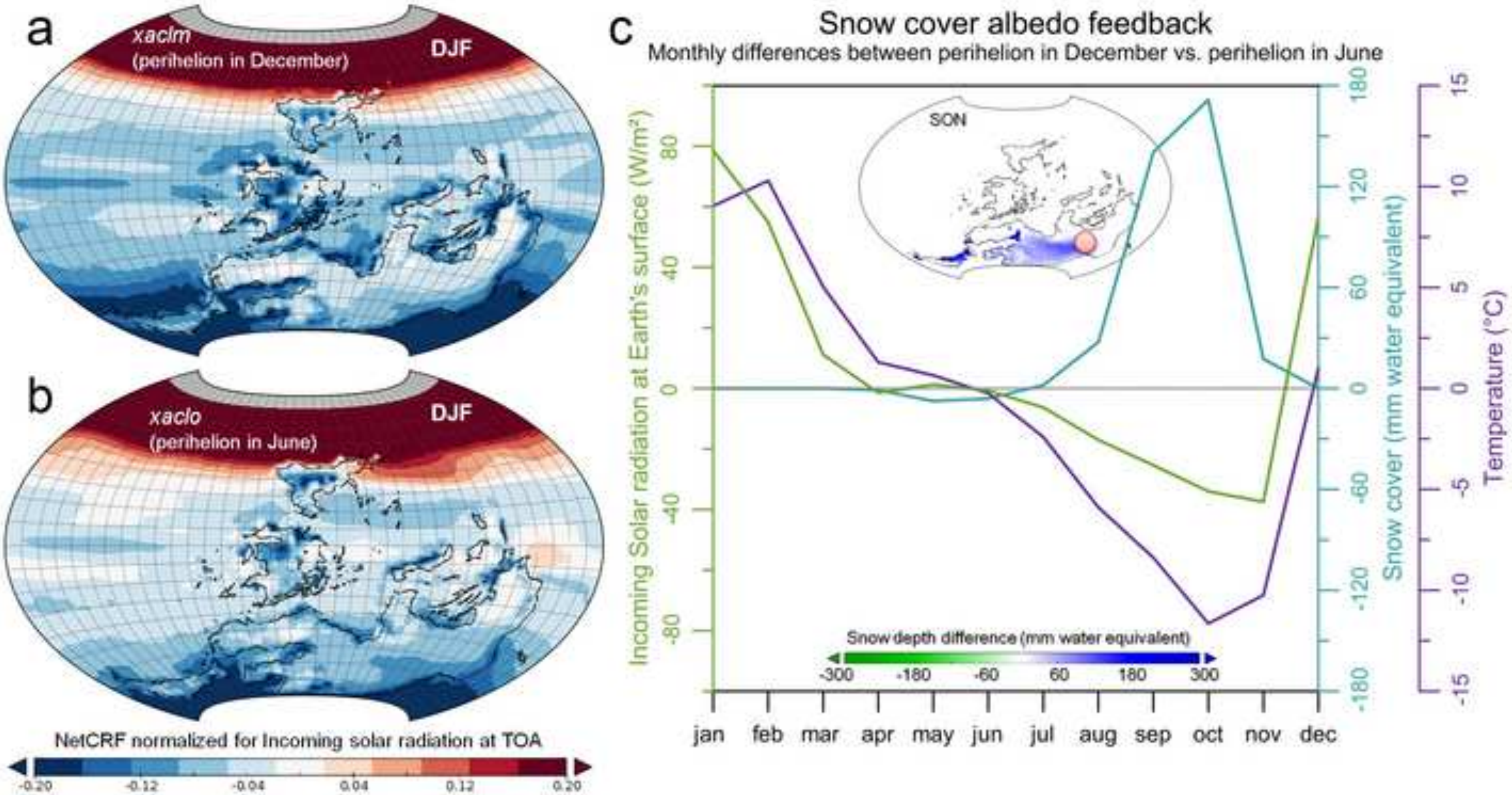

Figure11
Click here to download high resolution image

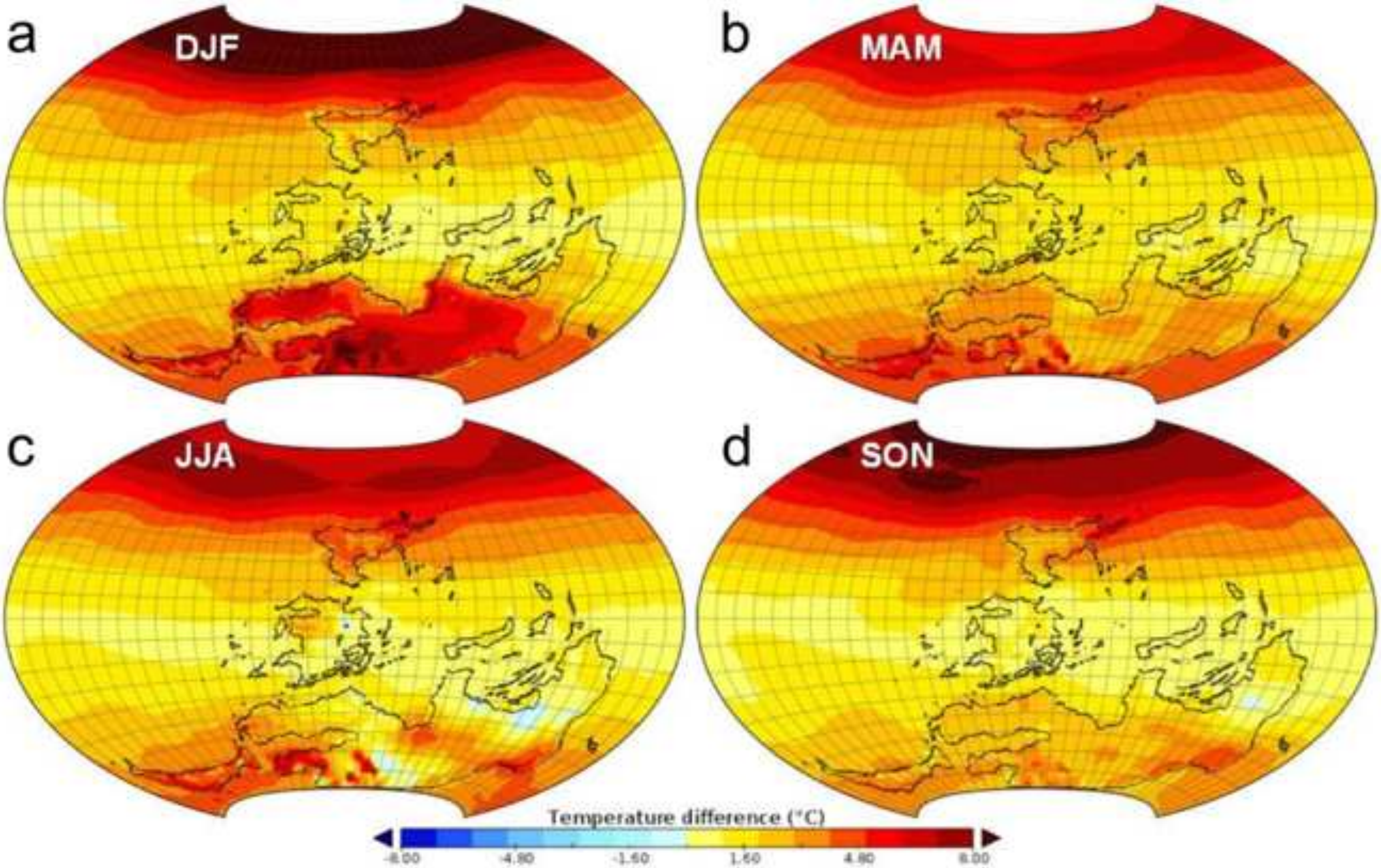

Figure12
Click here to download high resolution image

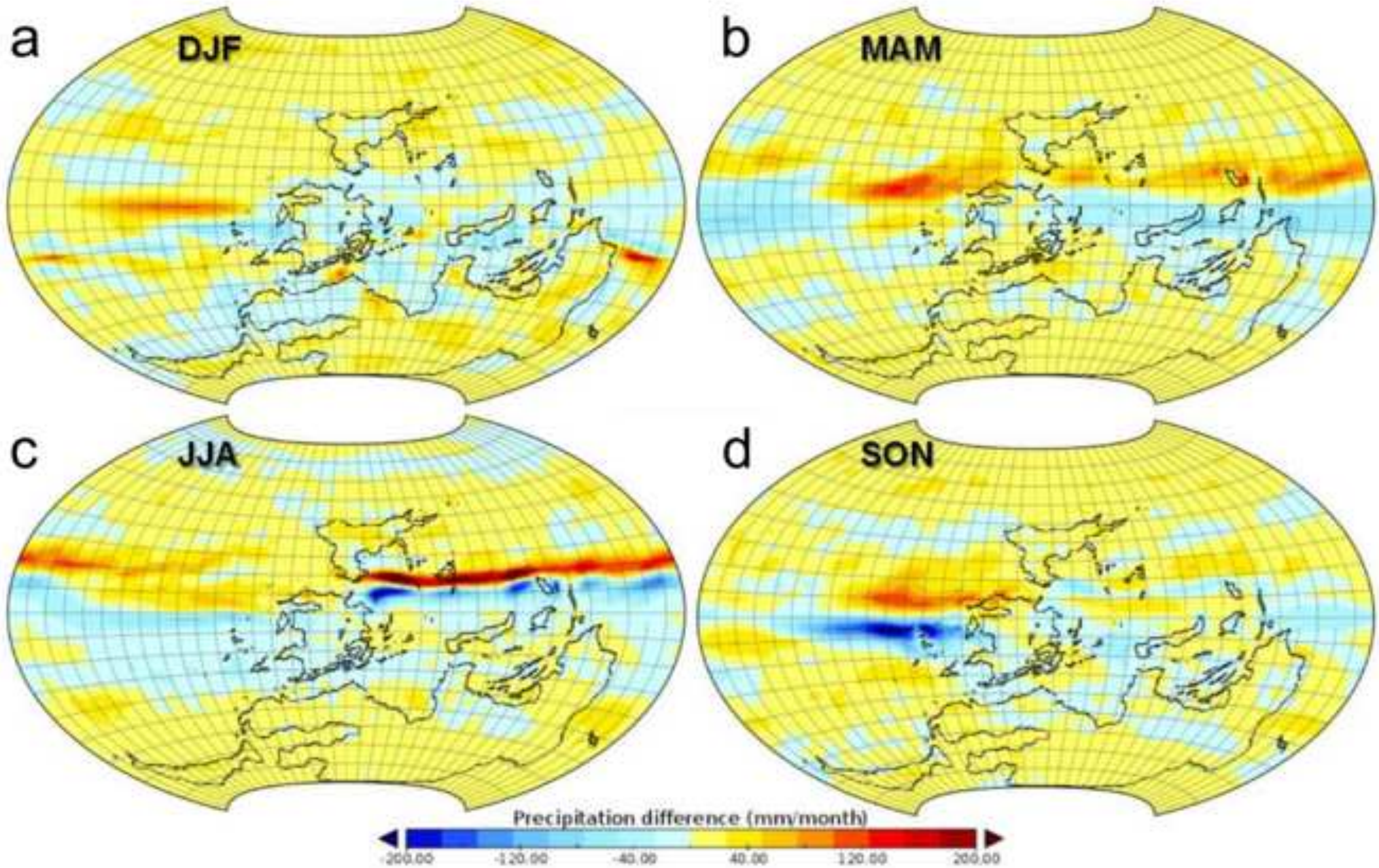

Figure13
Click here to download high resolution image

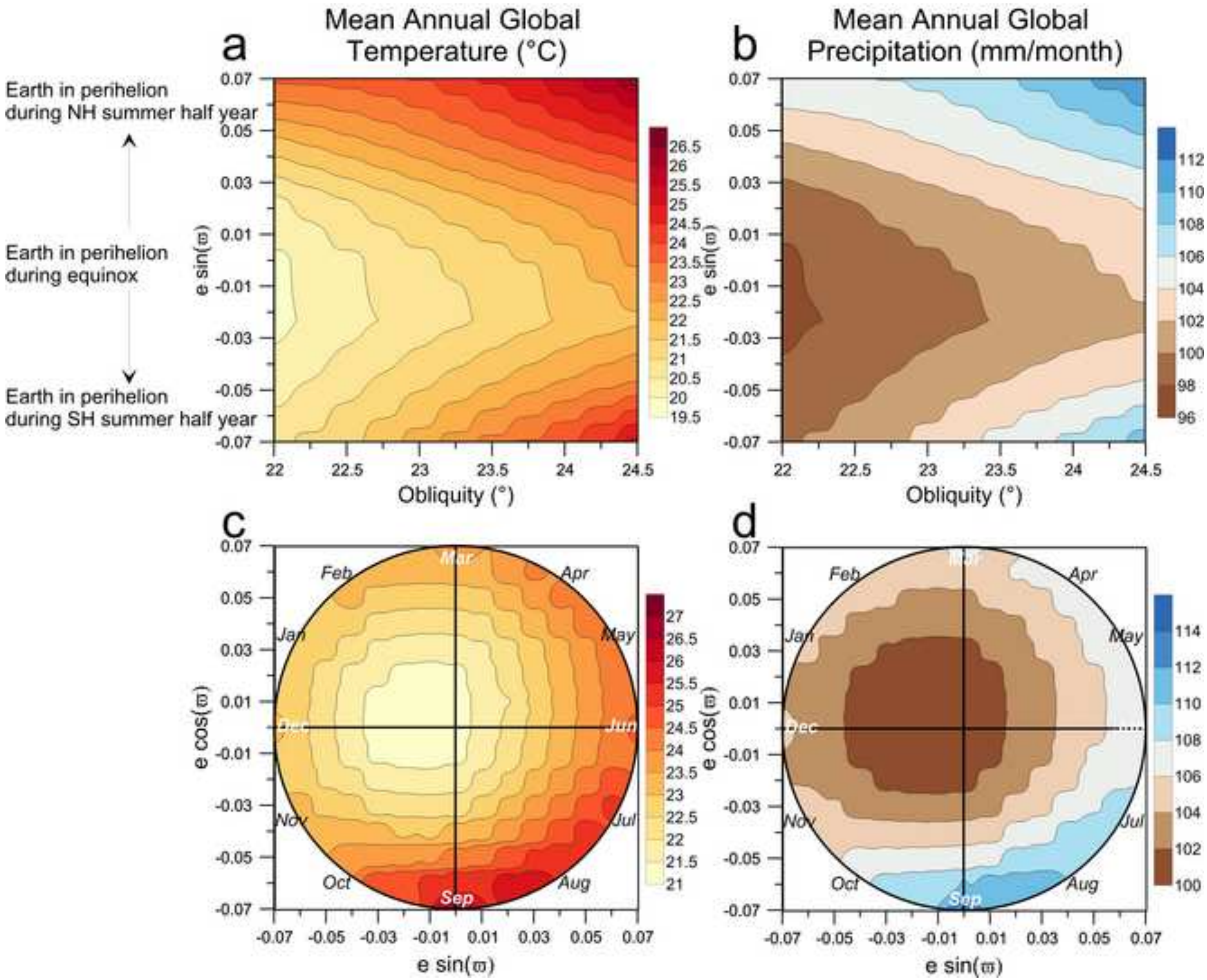

Figure14

Click here to download high resolution image

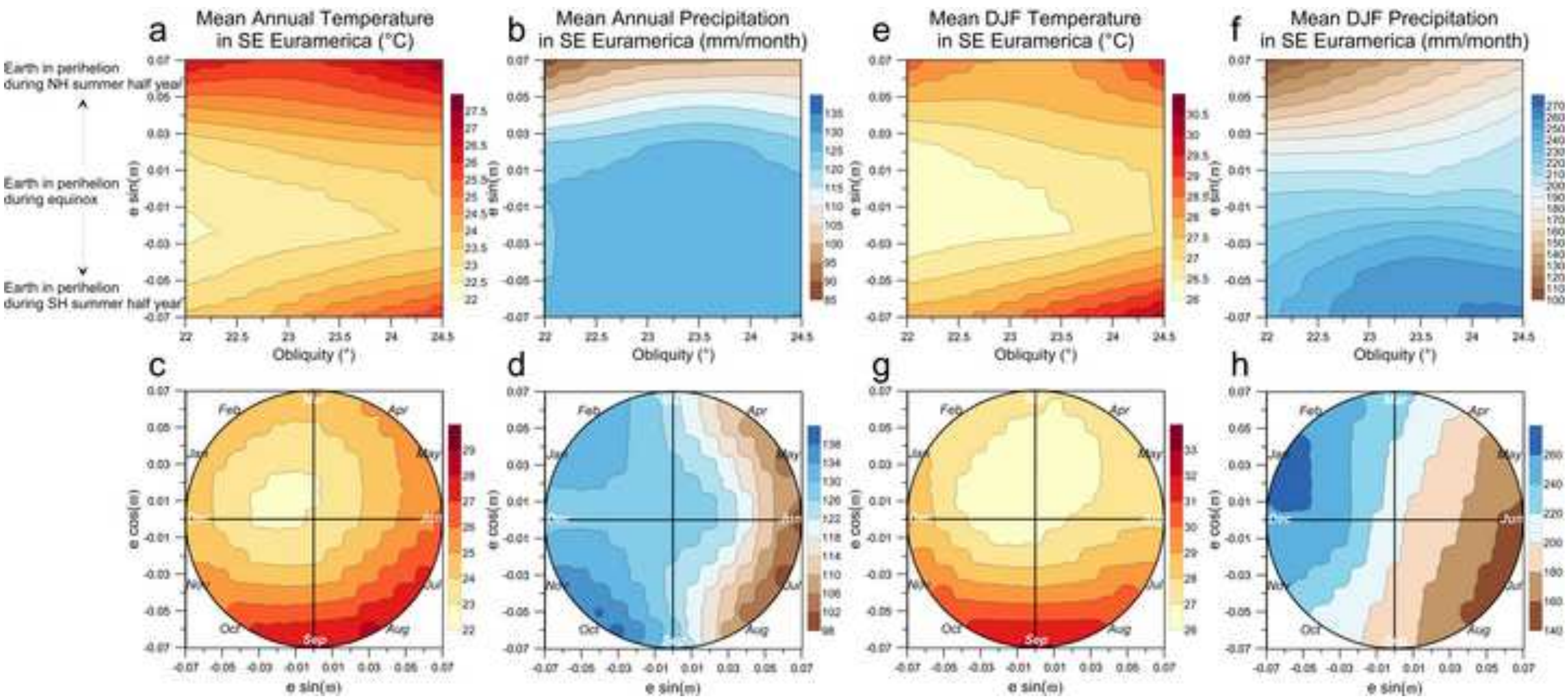

Figure15

Click here to download high resolution image

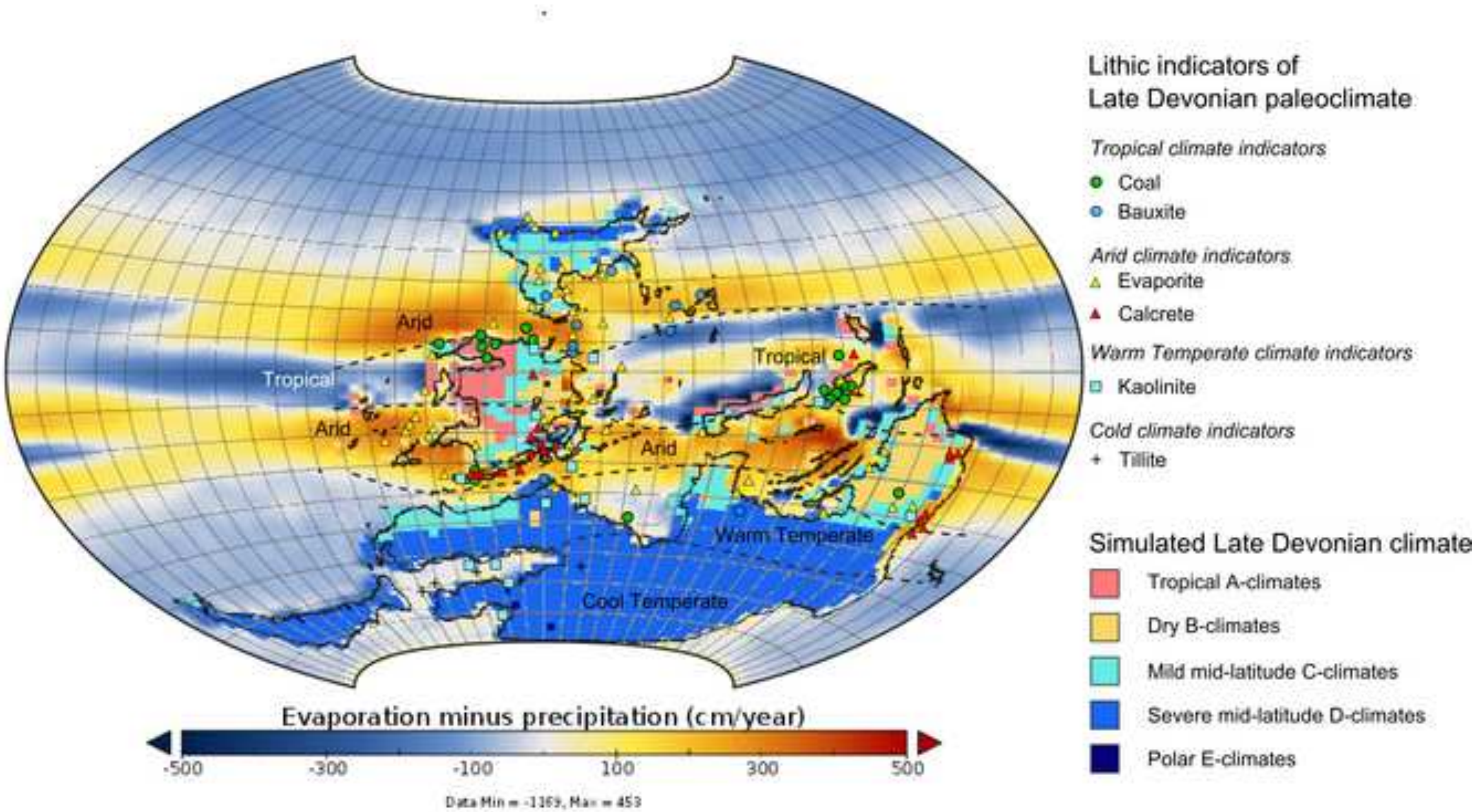

Figure16

Click here to download high resolution image